Chapter 11 - BATHYMETRIC ESTIMATION

David T. Sandwell
University of California, San Diego
Scripps Institution of Oceanography
La Jolla, CA 92093-0225

Walter H. F. Smith
NOAA, Laboratory for Satellite Altimetry
Silver Spring, MD 20910-3282

7 January 1999
(To appear in *Satellite Altimetry and Earth Sciences*, Academic Press, 1999)
Revised: 7 July 1999

ABSTRACT

The surface of the ocean bulges outward and inward reflecting the topography of the ocean floor. A dense mapping of ocean surface topography from declassified Geosat altimeter data (US Navy), ERS-1 altimeter data (European Space Agency), and repeat-track coverage from the Topex/Poseidon altimeter (NASA and CNES) has provided the first view of the ocean floor structures in many remote areas of the Earth. The spatial resolution of the derived gravity field is limited by travel-time noise from ocean waves and can be improved through additional dense measurements. Altimeter-derived gravity can be used to estimate seafloor topography but only over an intermediate wavelength band ($200 < \lambda < 20$ km) and only in areas where sediment cover is thin. The longer wavelength variations in depth are constrained by depth soundings collected by research vessels over the past 30 years. Detailed bathymetry is essential for understanding physical oceanography, marine geophysics, and perhaps even biological oceanography. Currents and tides are controlled by the overall shapes of the ocean basins as well as the smaller sharp ocean ridges and seamounts. Because erosion rates are low in the deep oceans, detailed bathymetry reveals the mantle convection patterns, the plate boundaries, the cooling/subsidence of the oceanic lithosphere, the oceanic plateaus, and the distribution of off-ridge volcanoes.

I. INTRODUCTION

A detailed knowledge of topography is fundamental to the understanding of most Earth processes. On the land, weather and climate are controlled by topography on scales ranging from large continental landmasses to small mountain valleys. Since the land is shaped by tectonics, erosion, and sedimentation, detailed topography is essential for any geological investigation. In the oceans, detailed bathymetry is also essential for understanding physical oceanography, biology, and marine geology. Currents and tides are controlled by the overall shapes of the ocean basins as well as by the smaller sharp ocean ridges and seamounts. Sea life is abundant where rapid changes in ocean depth deflect nutrient-rich water toward the surface. Because erosion and sedimentation rates are low in the deep oceans, detailed bathymetry also reveals the mantle convection patterns, the plate boundaries, the cooling/subsidence of the oceanic lithosphere, the oceanic plateaus, and the distribution of off-ridge volcanoes.

Topographic mapping with orbiting laser and radar altimeters has been the focus of current exploration of Venus, the Moon, and Mars and is providing very high resolution topographic maps of the Earth's land areas. However, since one cannot directly map the topography of the ocean basins from space, most seafloor mapping is a tedious process that has been carried out over a 30-year period by research vessels equipped with single or multibeam echo sounders [*Canadian Hydrographic Office*, 1981]. For example, a complete mapping of the ocean basins at 100-m horizontal resolution would take about 125 ship-years of survey time using the latest multibeam technology. Oddly, some of the most valuable depth measurements of remote ocean areas were collected prior to satellite navigation and shipboard computer facilities and thus the quality of the data is highly non-uniform [*Smith*, 1993]. Moreover, many of the dense surveys of the northern oceans remain classified in military archives [*Medea*, 1995] or remain proprietary for economic or political reasons. Thus, until recently, our knowledge of the seafloor topography was poor except along the spreading ridge axes where there is almost complete coverage from the RIDGE program.

Two developments have vastly improved our knowledge of seafloor topography. First, the careful efforts by scientists throughout the world [*Canadian Hydrographic Office*, 1981] to archive the digital sounding data and assemble the data into large databases has provided much improved access to the 30-year mapping effort [*Wessel and Watts*, 1988; *Smith*, 1993]. Second, radar altimeters aboard the ERS-1 and Geosat spacecraft have surveyed the marine gravity field over nearly all of the world's oceans to a high accuracy and moderate spatial resolution. In March of 1995, ERS-1 completed its dense mapping (~8 km track spacing at the equator) of sea surface topography between latitudes of $\pm$ 81.5˚. Moreover in July of 1995, all of the high-density radar altimeter data collected by the Geosat spacecraft were declassified. These data have been combined and processed to form a global marine geoid or gravity grids [*Cazenave et al.*, 1996; *Sandwell and Smith*, 1997; *Tapley and Kim*, Chapter 10]. In the wavelength band 15 to 200 km, variations in

gravity anomaly are highly correlated with seafloor topography and thus, in principal, can be used to recover topography. As described in this chapter there are ongoing efforts to combine ship and satellite data to form a uniform-resolution grid of seafloor topography [*Baudry and Calmant,* 1991; *Jung and Vogt,* 1992; *Calmant,* 1994; *Smith and Sandwell,* 1994; *Sichoix and Bonneville,* 1996; *Ramillien and Cazenave,* 1997; *Smith and Sandwell,* 1997] . The sparse ship soundings constrain the long wavelength variations in seafloor depth and are also used to calibrate the local variations in topography to gravity ratio associated with varying tectonics and sedimentation. The satellite-derived gravity anomaly provides much of the information on the intermediate to short wavelength topographic variations (160-20 km).

The basic theory for predicting seafloor topography from satellite altimeter measurements is nicely summarized in a paper by *Dixon et al.* [1983]. Models of flexurally compensated seafloor topography have been used to develop a spectral transfer function for projecting seafloor topography into gravity anomaly (or geoid height) [*McKenzie and Bowin,* 1976; *Banks et al.*, 1977; *McNutt,* 1979; *Ribe,* 1982]. The important parameters are the crustal density, the mean ocean depth, and the thickness of the elastic portion of the lithosphere. The inverse of this transfer function provides a theoretical basis for projecting gravity anomaly measurements into seafloor topography but there are a number of complications that require careful treatment. 1) The gravity to topography transfer function becomes singular at both short wavelengths ($\lambda << 2\pi$ times mean ocean depth) and long wavelengths ($\lambda >>$ depth of compensation or flexural wavelength) due to upward continuation and isostatic compensation, respectively (Figure 1). Thus bathymetric prediction is only possible over a limited band. 2) While the short wavelength portion of the gravity to topography transfer function depends on well known parameters (ocean depth, crustal density), the longer wavelength portion is highly dependent on the elastic thickness of the lithosphere and/or crustal thickness. 3) Sediments raining down onto the seafloor preferentially fill bathymetric lows and can eventually completely bury the pre-existing basement topography. This adds a spatially dependent and non-linear aspect to the gravity-to-topography transfer function. 4) The transfer function is two-dimensional although usually it is assumed to be isotropic. Thus complete ocean surface gravity coverage is required. 5) Finally, in areas where the amplitude of the topographic relief approaches the mean depth, the transfer function is inherently non-linear [*Parker,* 1973]. Many previous studies have identified and addressed some of these issues [*Dixon et al.,* 1983; *Baudry and Calmant,* 1991; *Jung and Vogt,* 1992; *Smith and Sandwell,* 1994; *Sichoix and Bonneville,* 1996].

II. GRAVITY ANOMALY AND SEA SURFACE SLOPES

As we will see in the next section in greater detail, the accurate recovery of seafloor topography at short wavelengths is critically dependent on the accuracy of the short wavelength gravity field

derived from satellite altimetry. As described in Chapters 1 and 10, a satellite altimeter measures the topography of the ocean surface which, to a first approximation, is a measure of geoid height or gravitational potential. The oceanographic studies described in earlier chapters use the deviations in sea surface height above or below the geoid to investigate currents, tides, and waves. These oceanographic signals are our error sources [*Rapp and Yi,* 1997] and therefore to understand the magnitude of the errors one must review how gravity anomalies are computed from noisy satellite altimeter measurements.

A. *Geoid Height, Vertical Deflection, Gravity Gradient, and Gravity Anomaly*

The geoid height $N(\mathbf{x})$ and other measurable quantities such as gravity anomaly $\Delta g(\mathbf{x})$ are related to the gravitational potential $V(\mathbf{x},z)$ [*Heiskanen and Moritz,* 1967]. Since we are primarily interested in short wavelength anomalies, we assume that all of these quantities are deviations from a spherical harmonic reference earth model [e.g., EGM96, *Lemoine et al.,* 1998] so a planar approximation can be used for the gravity computation. In the following equations, the bold **x** denotes the coordinate (x,y); similarly **k** denotes (k_x,k_y) where $k_x = 1/\lambda_x$,where λ_x is wavelength. To a first approximation, the geoid height is related to the gravitational potential by Brun's formula,

(1)

$$N(\mathbf{x}) \quad \frac{1}{g_o} V(\mathbf{x},0)$$

where g_o is the latitude-dependent, average acceleration of gravity (~9.8 m s^{-2}). The gravity anomaly is the vertical derivative of the potential,

(2)

$$\Delta g(\mathbf{x}) = -\frac{\partial V(\mathbf{x},0)}{\partial z}$$

the east component and north component of vertical deflection are the slope of the geoid in the x- and y-directions, respectively

(3)

$$\eta(\mathrm{x}) \quad \frac{-1}{g_o}\frac{\partial V}{\partial x}, \qquad \xi(\mathrm{x}) \quad \frac{-1}{g_o}\frac{\partial V}{\partial y}$$

These quantities are related to one another through Laplace's equation.

(4)

$$\frac{\partial^2 V}{\partial x^2} + \frac{\partial^2 V}{\partial y^2} + \frac{\partial^2 V}{\partial z^2} = 0$$

Following *Haxby et al.* [1983] the differential equation (4) is reduced to an algebraic equation by fourier transformation

$$\Delta g(\mathbf{k},0) = \frac{ig_o}{|\mathbf{k}|}\left[k_x \eta(\mathbf{k}) + k_y \xi(\mathbf{k})\right] \tag{5}$$

To compute gravity anomaly from a dense network of satellite altimeter profiles of geoid height, one first constructs grids of east η and north ξ vertical deflection. The grids are then fourier transformed and Eq. (5) is used to compute gravity anomaly [*Sandwell*, 1992]. At this point one could also add the spherical harmonic gravity model back to the gridded gravity values in order to recover the long wavelength gravity field. A more complete description of gravity field recovery from satellite altimetry can be found in [*Hwang and Parsons*, 1996; *Sandwell and Smith*, 1997; *Rapp and Yi*, 1997]. The important issue for bathymetric estimation is revealed by a simplified version of Eq. (5). Consider the sea surface slope and gravity anomaly across a two-dimensional structure. The *y*-component of slope is zero so conversion from sea surface slope to gravity anomaly is simply a Hilbert transform.

$$\Delta g(\mathbf{k},0) = ig_o \,\mathrm{sgn}(k_x)\eta(\mathbf{k}) \tag{6}$$

Now it is clear that one μrad of sea surface slope maps into 0.98 mGal of gravity anomaly and similarly one μrad of slope error will map into 1 mGal of gravity anomaly error. Thus the accuracy of the gravity field recovery and hence the accuracy of the bathymetric prediction is controlled by the accuracy of the sea surface slope measurement, especially the short-wavelength slope estimates.

III. LIMITATIONS OF RADAR ALITMETRY FOR GRAVITY FIELD RECOVERY

As described in Chapter 1 and in section VIII (Appendix), a satellite altimeter uses a pulse-limited radar to measure the altitude of the satellite above the closest sea surface point. Global precise tracking, coupled with orbit dynamic calculations provide an independent measurement of the height of the satellite above the ellipsoid. The difference between these two measurements is equal to the sea surface height (~geoid height) minus any delays in the propagation of the radar echo due to the ionosphere and troposphere. There are many errors in these measurements but most occur over length scales greater than a few hundred kilometers [*Chapter* 1 *and* 10; *Sandwell*, 1991; *Tapley et al.*, 1994]. For gravity field recovery and bathymetric estimation, the major error source is the roughness of the ocean surface due to ocean waves. The radar pulse reflects from an

area of ocean surface (footprint) that grows with increasing sea state [see *Stewart,* 1985 and section VIII]. The superposition of the reflections from this larger area stabilizes the shape of the echo but it also smoothes the echo so that the timing of its leading edge less certain. By averaging many echoes (1000 Hz) over multiple repeat cycles one can achieve a 10-20 mm range precision [*Noreus* 1995; *Yale et al.*, 1995]. Over a distance of 4 km (i.e. 1/4 wavelength) this corresponds to a sea surface slope error of 4 μrad which maps into a gravity error of about 4 mGal. Thus the only way to improve the resolution is to make many more measurements or stop the ocean waves!

This situation is compounded in the deep oceans (~4000 m) because upward continuation of the gravity field from the ocean floor to the ocean surface provides a strong low-pass filter on the gravity signal (Figure 1) but has no effect on the radar noise. Consider an anomaly on the ocean floor with an 16 km wavelength and a 15 mGal amplitude (i.e., a typical value for oceans). On the ocean surface this anomaly will be reduced to 3.1 mGal by upward continuation.

Other sources of error include tide model error, ocean variability, mean ocean currents, ionospheric delay, tropospheric delay, and electromagnetic bias. Corrections for many of these errors are supplied with the geophysical data record. However, for gravity field recovery and especially bathymetric prediction not all corrections are relevant or even useful. For example, corrections based on global models (i.e., wet troposphere, dry troposphere, ionosphere, and inverted barometer) typically do not have wavelength components shorter than 1000 km, and their amplitude variations are less than 1 m so they do not contribute more than 1 μrad of error. In addition, the corrections can sometimes have steps associated with geographical boundaries; the numerical derivative of even a 10 mm step will introduce significant noise in the slope estimate. *Yale*, [1997] has examined the slope of the corrections supplied with the Topex/Poseidon GDR and found only the tide correction [*Bettadpur and Eanes*, 1994] should be applied . The dual frequency altimeter aboard Topex/Poseidon satellite provides an estimate of the ionospheric correction, however, because it is based on the travel time difference between radar pulses at C-band and Ku-band, the noise in the difference measurement adds noise to the slope estimate for wavelengths less than about 100 km [*Imel*, 1994]. The most troublesome errors are associated with mesoscale variability and permanent dynamic topography [*Rapp and Yi,* 1997]. The variability signal can be as large as 6 μrad but fortunately it is confined to a few energetic areas of the oceans and given enough redundant slope estimates from nearby tracks [*Sandwell and Zhang*, 1989], some of this noise can be reduced by averaging. Permanent dynamic topography can have slope up to 6 μrad; this will corrupt both the gravity field recovery and the bathymetric prediction over length scales of 100-200 km.

IV. FORWARD MODELS

The forward relationship between topography and gravity anomaly is best described in the two-dimensional fourier transform domain. First consider the case of uncompensated seafloor topography of density ρ_c lying at an average depth of d beneath the ocean surface. Let $h(\mathbf{x})$ be the topography of the seafloor with respect to this mean ocean depth. The exact formula for the gravity anomaly Δg due to the topography is [*Parker*, 1973]

$$F[\Delta g] = 2\pi\Gamma(\rho_c - \rho_w)\exp[-2\pi|\mathbf{k}|d]\sum_{n=1}^{\infty}\frac{|2\pi\mathbf{k}|^{n-1}}{n!}F[h^n(\mathbf{x})] \tag{7}$$

where $F[]$ is the two-dimensional Fourier transform operator, Γ is the Newtonian gravitational constant, and ρ_w is the density of seawater. When the topography lies well below the plane of the gravity observations (i.e., sea level), this series converges quite rapidly. Moreover if the maximum amplitude of the topography is much less than the mean ocean depth, then the first term in the series dominates. Indeed it is common to use only the first term because it provides a linear isotropic relationship between the fourier transform of the gravity anomaly $\Delta G(\mathbf{k})$ and the fourier transform of the topography $H(\mathbf{k})$.

$$G(\mathbf{k}) = 2\pi\Gamma(\rho_c - \rho_w)\exp[-2\pi|\mathbf{k}|d]H(\mathbf{k}) \tag{8}$$

The model is appropriate for all types of topography (e.g., seamounts, fracture zones, trenches).

Next consider a more realistic model where the lithosphere flexes downward in response to the load of the topography. The simplest model consists of a thin elastic plate overlying a fluid asthenosphere [*McKenzie and Bowin*, 1976; *Banks et al.*, 1977; *McNutt*, 1979]. Note this model also applies to all types of seafloor topography (e.g., seamounts, fracture zones and trenches) as long as the features are not obscured by sediments. As the plate flexes downward (or upward), it displaces the crust-mantle boundary that provides an isostatic restoring force. Assuming thin elastic plate flexure with isotropic and spatially invariant response, the deflection of the crust/mantle interface $M(\mathbf{k})$ is related to the surface topography

$$M(\mathbf{k}) = -\left(\frac{\rho_c - \rho_w}{\rho_m - \rho_c}\right)\Phi(|\mathbf{k}|)H(\mathbf{k}) \tag{9}$$

where ρ_m is the density of the mantle and the isostatic response function Φ is given by

(10)

$$\Phi(|\mathbf{k}|) = \left[1 + (\lambda|\mathbf{k}|)^4\right]^{-1}$$

The characteristic wavelength of the flexure $\lambda = 2\pi[D/g(\rho_m - \rho_c)]^{1/4}$ depends on the elastic thickness of the lithosphere which in turn depends on the age of the lithosphere at the time the topography formed [*Watts*, 1978; *Wessel* 1992]. This flexural wavelength can vary from 100 to 800 km depending on tectonic conditions. Moreover, since nearby topographic features such as seamounts can have completely different flexural characteristics, the spatially varying flexural wavelength introduces a major complication in bathymetric estimation. Nonetheless the flexure model provides a theoretical framework for the design of downward continuation, low-pass, and high-pass filters used in bathymetric prediction [*Dixon et al.*, 1983; *Baudry and Calmant*, 1991; *Smith and Sandwell*, 1994].

The deflection of the crust/mantle interface introduces a second contribution to the gravity anomaly. Again neglecting the non-linear terms in the Parker expansion (Eq. (7)) there is an isotropic transfer function, or admittance function, *Z* for mapping seafloor topography into sea surface gravity anomaly.

(11)

$$G(\mathbf{k}) = 2\pi\Gamma\left(\rho_c - \rho_w\right)\exp\left[-2\pi|\mathbf{k}|d\right]\left[1 - \Phi(|\mathbf{k}|)\exp\left(-2\pi|\mathbf{k}|c\right)\right] H(\mathbf{k})$$

$$G(\mathbf{k}) = Z(|\mathbf{k}|)\, H(\mathbf{k})$$

Examples of this transfer function are shown in Figure 2 (upper). Before discussing the inverse of this transfer function and its role in bathymetric prediction, one should be aware of an additional complication due to sediments on the seafloor. Sediments generally accumulate long after the primary basement features are formed so they induce yet another topographic load and flexural response. The overall effects of sedimentation on the transfer function make it non-linear because sediments preferentially fill bathymetric lows and the sediment density varies with compaction depth. In the extreme case of complete burial, the gravity to basement topography ratio reverses sign so the basement high has a negative gravity anomaly; there is a well documented case in the Indian Ocean where the 85 Ridge is completely buried by the Bengal Fan [*Liu et al.*, 1982]. Of course when the sediments dominate, such as on the shallow continental margins, the topography is flat while the gravity reflects deeper structure; in these areas gravity anomaly is useless for predicting topography.

These limitations and assumptions of the flexural compensation model suggest that the gravity-to-topography transfer function Eq. (11) is only approximate and can only be used in ideal

situations. The primary importance of the model is to reveal fundamental limitations in the mapping from gravity anomaly to topography. In the ideal situation one could construct a topographic grid by inverting Eq. 11.

$$G(\mathbf{k}) = Z(|\mathbf{k}|)^{-1} H(\mathbf{k}) \tag{12}$$

A plot of Z^{-1} for two flexural wavelengths and a typical ocean depth of 4 km, illustrates the three problems (Figure 2 - lower). 1) The inverse transfer function increases exponentially for wavelengths less than 50 km so, for example, at a wavelength of 19 km, 4 mGal of gravity noise will map into 200 m of bathymetric estimation error. Since seafloor has about 200 m of rms relief, the noise begins to dominate the signal at these short wavelengths. 2) The transfer function grows rapidly at long wavelengths because isostatic compensation causes a near perfect cancellation between the gravity from the topography and the gravity from the relief on the crust/mantle interface; again any noise will be amplified. 3) The more important issue at long wavelengths is that the topography-to-gravity ratio is very sensitive to the flexural wavelength, and, since this is an unknown parameter that can vary significantly between, for example, a young seamount near an old fracture zone it introduces a major uncertainty in the prediction. The critical issue is that there is a band of wavelengths where ocean surface gravity can be used to estimate topography but prediction outside this band should be avoided. Other measurements such as ship soundings can be used to recover the long wavelengths. Short-wavelength bathymetry can only be efficiently recovered with multibeam swath surveys.

V. INVERSE APPROACHES

Here we review the various inverse approaches that are used overcome these fundamental limitations. Since there is no one "correct" method and the practical implementation is a matter of taste, one may call these *recipes*. The first part of the recipe, which is common to all approaches, is to use available ship soundings and other depth information to construct a long-wavelength model of the ocean basin and then remove this long-wavelength field from available depth soundings. To be consistent one should remove the same long-wavelength components from the gravity field. The long-wavelength topography is then restored as a final step in the recipe; this is called a *remove/restore* procedure.

The basic spectral approach (Eq. 12) overcomes the inherent singularities at long and short wavelengths by *windowing* the inverse transfer function. Window shapes range from a simple boxcar [*Dixon et al.,* 1983] to more complicated functions based on the signal and noise properties of the gravity field and the mean ocean depth [*Smith and Sandwell,* 1994; *Sichoix and Bonneville,*

1996]. The amplitude and shape of the inverse transfer function depends on the density of the crust and the flexural wavelength, respectively. Some investigators vary these parameters to obtain a good match to known depth soundings [*Baudry and Calmant,* 1991; *Jung and Vogt,* 1992; *Calmant,* 1994; *Sichoix and Bonneville,* 1996; *Ramillien and Cazenave,* 1997] while others vary just the crustal density and avoid the compensation issue by eliminating all signals in the compensation band [*Smith and Sandwell,* 1994; *Smith and Sandwell,* 1997]. Moreover, if the compensation band is eliminated, one can downward-continue the gravity field to the mean ocean depth; this flattens the inverse transfer function so that, in the space domain, a plot of topography versus gravity should lie on a straight line with the slope related to the crustal density. *Nettleton* [1939] used this approach to estimate density from measurements of gravity and topography so we call this the *inverse Nettleton procedure* [*Smith and Sandwell,* 1994].

These spectral methods neglect the non-linear terms in the relationship between topography and gravity (7). These terms are important for tall seamounts, especially when they pierce the ocean surface. *Calmant* [1994] uses an entirely space-domain approach where the non-linear terms are included. His approach appears to work best for small regions where a few ship soundings are available for calibration and may also be best for a global solution although it is computationally expensive. *Smith and Sandwell* [1997] have added an additional step to the spectral/Nettleton approach to force agreement with shipboard depth measurements. In this final step, the predicted depths are subtracted from known depth soundings. The difference is gridded using a minimum curvature approach [*Smith and Wessel,* 1990] and finally the difference grid is added back to the prediction grid. This processes insures that the final grid matches known soundings exactly and blends smoothly into areas where the gravity field provides the only estimates of topography; we call this *polishing the grid* since it makes things look nice and it can be done over and over again as new depth soundings become available.

A final untested method is the so-called *linear inverse theory* approach [*Parker,* 1994]. Assume that gravity and topography are linearly related such that the topography $h(\mathbf{x})$ is equal to the gravity anomaly $\Delta g(\mathbf{y})$ convolved over with an unknown linear, isotropic transfer function $q(|\mathbf{x} - \mathbf{y}|)$.

(13)

$$h(\mathbf{x}) = \iint_A q(|\mathbf{x} - \mathbf{y}|)\,\Delta g(\mathbf{y})\,d^2\mathbf{y}$$

or

$$h(\mathbf{x}) = \iint_A q(|\mathbf{y}|)\,\Delta g(\mathbf{x} - \mathbf{y})\,d^2\mathbf{y}$$

After changing the **y**-variable of integration from Cartesian coordinates to cylindrical coordinates, the convolution integral becomes:

$$h(x_1, x_2) = \int_0^{\infty} r q(r) \left[\int_0^{2\pi} \Delta g(x_1 - r\cos\theta, x_2 - r\sin\theta) d\theta \right] dr \tag{14}$$

Given complete 2-dimensional gravity anomaly measurements, the integration in brackets can be performed numerically for any values of x_1, x_2 and r; we'll call this function $G(x_1, x_2, r)$. Finally the convolution integral can be written as:

$$h(x_1, x_2) = \int_0^{\infty} q(r) G(x_1, x_2, r) r \, dr \tag{15}$$

We can view this as a standard linear inverse problem for the function $q(r)$ [*Parker,* 1994]. Bathymetric soundings along isolated ship tracks provide values of $h(\mathbf{x})$ on the left side of the equation and the very dense satellite maps allow us to calculate the kernel function G for every depth sounding. Standard linear inversion techniques can be used to estimate $q(r)$. Finally, once $q(r)$ is known, one can use Eq. (13) to compute the topography from the gravity in the areas between the depth soundings.

The advantage of this method is that in addition to estimating the topography, one can also estimate the uncertainty of the topography in the interpolated areas. Moreover, the transfer function $q(r)$ contains geologic information such as the mean crustal thickness and the flexural wavelength of the lithosphere when the topography formed.

VI. DATA AVAILABILITY AND CASE STUDY: BATHYMETRIC ESTIMATION

Ship soundings were assembled from a variety of sources. In all cases we used only the center beam from multibeam surveys in order to match the single-beam coverage of the older cruise data. We thank many scientists who provided us with soundings from their very recent cruises; these cruises were largely guided by the satellite gravity observations and thus cover some of the more interesting and high relief features in the ocean basins. In particular cruise data from the Pacific Antarctic and Southeast Indian ridges filled some important gaps in ship coverage. Archive data were derived from 4 overlapping sources. The most important contributions were originally archived at Lamont Doherty Earth Observatory where, over the years, scientists inspected data, corrected blunders, and digitized analog soundings that were acquired prior to digital recordings. Two databases were derived from the original Lamont data. The *Wessel and Smith* (WS) data

base was organized, cleaned, and placed in an easily assessable GMT format to investigate the quantity and quality of marine gravity [*Wessel and Watts,* 1988] and marine bathymetry [*Smith,* 1993]. During his assessment of the data, Smith rescued bad sounding lines that contained obvious but fixable problems such as incorrect units or conversion factors and identified cruises where soundings were hopelessly bad. The *Brown Book* (BB) data base was also converted to a GMT format and contains almost all of the cruises found in the WS database. It is largely optimized for investigations of marine magnetic anomalies but it has also been augmented with many unique or recent cruises to the Southern Ocean. Steven Cande (personal communication, 1995) provided us with complete access to these BB data for our project. The most complete database has been assembled by the *National Geophysical Data Center* (NGDC) in their Geodas-3 CD [1995]. The NGDC database contains many cruises not found in the Lamont-derived databases; these were contributed by other institutions throughout the world. While the NGDC data are more complete, there has been no attempt to clean and rescue bad sounding lines and therefore the original Lamont-derived data provide a more reliable contribution. Finally, the *Scripps Institution of Oceanography* (SIO) database was included to ensure that no important cruises or very recent cruises were omitted. The four data bases were inserted into a common GMT-Plus data format at the SIO Geological Data Center using the data base methods developed at Lamont [*Wessel and Watts,* 1988; *Smith,* 1993].

The compilation of the satellite-derived gravity anomaly grid is described in a recent publication [*Sandwell and Smith,* 1997]. Along track sea surface slopes from 4.5 years of Geosat and 2 years of ERS-1 and were used to construct a global marine gravity grid with cell dimensions of 2 minutes in longitude and cos(latitude) times 2 minutes in latitude so that cells are equidimensional but vary in size with latitude. The higher accuracy profiles come from averages of 16 ERS-1 repeat cycles along its 35-day repeat track and up to 66 Geosat repeat cycles along its 17-day repeat track. The higher spatial density profiles come from the 1.5-year Geosat Geodetic Mission and the 1-year ERS-1 Geodetic Mission [Figure 3]. Away from coastlines, the accuracy of the resulting gravity grid is 3-7 mGal depending on factors such as local sea state and proximity to areas of high mesoscale ocean variability [*Marks,* 1996; *Sandwell and Smith,* 1997]. As discussed above, the accuracy and resolution of the bathymetric prediction are highly dependent on the accuracy of the gravity anomaly grid.

Our method of forming a grid of seafloor topography from these data follows the approach of *Smith and Sandwell* [1994; 1997].

1) Grid available bathymetric soundings on the 2 minute Mercator grid between latitudes of $\pm 72^{\circ}$. Coastline points from GMT [*Wessel and Smith,* 1996] provide the zero-depth estimates. A finite-difference, minimum-curvature routine is used to interpolate the global grid [*Smith and Wessel,* 1990].

2) Separate the bathymetry grid into *low-pass* and *high-pass* components using a Gaussian filter (0.5 gain at 160 km). Filtering and downward continuation are performed with a multiple strip, 2-D FFT that spans 0-360˚ longitude to avoid Greenwich edge effects.
3) Form *high-pass filtered gravity* using the same Gaussian filter.
4) Downward continue the *high-pass filtered gravity* to the *low-pass filtered bathymetry* assuming Laplace's equation is appropriate. A depth-dependent Wiener filter is used to stabilize the downward continuation.
5) Accumulate *high-pass filtered soundings* and corresponding *high-pass filtered/downward-continued gravity* into small (160 km) overlapping areas and perform a robust regression analysis. In sediment-free areas, where the relief is much less than the mean ocean depth, the topography/gravity transfer function should be flat and equal to $1/2\pi G\Delta\rho$ so in the space domain, a linear regression is appropriate. This works well where sediment cover is thin, such as young seafloor. Where regression shows a poor correlation between topography and gravity, we assume the seafloor is flat and set the *topography/gravity ratio* to zero. Finally there are intermediate cases where topographic depressions will be sediment filled while the highs protrude above the sediments so the topography/gravity relationship is non-linear. It is these partially sedimented areas that make the bathymetric problem difficult; continental margins and shelves pose similar problems. We believe that the non-linear effects due to sediment infill are more serious than the errors due to neglecting the non-linear terms in the gravity expansion Eq. (7).
6) Regional *topography/gravity ratio* estimates are gridded and multiplied by the *high-pass filtered/downward-continued gravity* to form *high-pass filtered predicted bathymetry*.
7) The *total predicted bathymetry* is equal to the sum of the *high-pass filtered predicted bathymetry* and the *low-pass filtered bathymetry*.
8) Finally, the pixels constrained by ship soundings or coastline data are reset to the measured values and the finite-difference, minimum curvature routine is used to perturb the predicted values toward the measured values (i.e. *polishing*). This final step (8) dramatically increases the accuracy and resolution of the bathymetric grid in well surveyed areas so it agrees with the best hand-contoured bathymetric charts. Grid cells where depth is constrained buy a sounding or coastline point are set to the nearest odd integer while predicted values are set to the nearest even integer; this encoding can be used to distinguish between measured and estimated depths. The grid is available by anonymous ftp (topex.ucsd.edu); high-resolution images can be copied from our web site (http://topex.ucsd.edu/mar_topo.html).

During the construction of the topography grid, additional bad cruise data became apparent as sharp tears in the imaged grid. These cruises were identified using two methods. First, after step 7) in the prediction sequence, the mean deviation and median absolute deviation between the measured and predicted depths were computed on a cruise-by-cruise basis. Higher than normal

differences indicated a problem with the cruise soundings, perhaps associated with a digitizing or scale-factor error. The second approach was to identify the bad cruise sounding data visually. Bad or suspect cruises were eliminated from the "good list" in the ship database and the entire prediction was re-done. Currently we are at revision 6.2 of this procedure and we expect to update the topography grid as more ship data become available or when the suspect cruise data can be repaired. Thus the grid is a living document that can improve with time.

VII. A. RESULTS, VERIFICATION, AND HYPSOMETRY

The results are shown in Figure 4 as a color image illuminated from the northwest. All of the familiar features of the ocean basins are apparent. The land topography from GTOPO30 is also included to provide a complete view of our planet. In the oceans, the continental margins are displayed as an orange-brown color. The seafloor spreading ridges stand out as broad highs (yellow to green to light blue) with an axial valley along the mid-Atlantic ridge and an axial high along the East Pacific Rise and the Pacific-Antarctic Rise. Fracture zones reflect the opening of the Atlantic basin while in the Pacific they record a more complex history of fast spreading and major reorganizations of the plates. Numerous seamounts, sometimes occurring in chains, record a complex history of off-axis volcanism. The deepest ocean basins (blue to purple) are also the oldest areas and their depth reflects cooling, thermal contraction, and isostatic subsidence of the oceanic lithosphere [*Parsons and Sclater,* 1977].

We have assessed the accuracy of the prediction through a comparison with soundings from a recent cruise to the Foundation Seamount Chain in the South Pacific (Figure 5.). This poorly charted area contains a 1600-km long volcanic chain as well as topography associated with microplate tectonics [*Mammerickx,* 1992]. Based on depth predictions from our earlier study [*Smith and Sandwell,* 1994], an initial mapping and sampling expedition was carried out in 1995 aboard the *R/V Sonne* [*Devey et al.*, 1997] where they charted 44 volcanoes with height ranging from 1500 m to 4000 m; eleven of the uncharted volcanoes come to within 500 m of the ocean surface. These *Sonne-100* sounding data were included in our global seafloor topography map and provide good definition of the summits of the seamounts (Figure 5a). In January and February of 1997, one of us (Sandwell) participated in a second expedition to the Foundation Seamounts area aboard *R/V L'Atalante* [*Maia et al.,* 1999]. The cruise track covers very high relief topography areas that were not surveyed during the *Sonne-100* cruise and thus offers an excellent test of the accuracy of the predicted seafloor depth. The results are shown in Figure 5b where the center beam of the Simrad 12D multibeam echo sounder is plotted versus distance from Tahiti (center profile). A number of large seamounts and ridges were surveyed between distances of 2500 and 4000 km while a 6500-m deep trench was surveyed at a distance of 5800 km. These measurements are compared with depths sampled from the ETOPO-5 grid (upper profile) and our

version 6.2 predicted depths (lower profile). The depths from ETOPO-5 show a poor correlation with the measured depths and have an rms misfit of 590 m in an area where the rms signal is large 747 m. The poor fit is due to a lack of ship soundings in the area. The prediction offers a much better match to the observed depths (259 m rms) because the high-resolution gravity field information from the Geosat and ERS-1 satellite altimeters provides most of the depth information. In other well charted areas of the northern oceans, the grid is more tightly constrained by ship soundings. On average, 12% of the grid cells are constrained by ship measurements while the remaining 88% are estimated.

One of the basic measurements of our planet, the hypsometry of the ocean floor (area vs. depth), was poorly constrained prior to this new solution (Figure 6). The earliest curves [e.g., *Menard and Smith*, 1961], calculated in 1 km intervals, show that most seafloor has a depth of 4-5 km. A more recent solution, ETOPO-5, cannot yield a more detailed curve because of biases toward multiples of 100, 200 and 500 m, the contours that were digitized to produce ETOPO-5. Our solution yields a smooth curve at 50 m intervals. Viewed in 1 km intervals, our solution has more area in the 3–4 km range and less in the 5–6 km range than was seen previously, reflecting the increased number of seamounts mapped by satellite altimetry. More importantly, the new hypsometry shows two peaks instead of just one. The deeper peak at 5100 m depth is a consequence of the flattening of the depth versus age relation [*Parsons and Sclater*, 1978; *Parsons*, 1982]. The shallower peak at 4200 m can be understood in terms of a global increase seafloor spreading during the 20–33 Ma period. Seafloor depth increases systematically as it ages [*Mueller et al*., 1997], cools, and becomes denser.

VII. B. EFFECTS ON OCEAN CURRENTS

Seafloor topography has a significant and perhaps dominant role in ocean circulation, especially at high latitudes. Vertical and horizontal ocean circulation can redistribute water masses, bringing them into contact with the atmosphere where they can buffer or drive regional and global climate change. Much of this water mass formation occurs in the Southern Ocean and especially along the frontal zone of the Antarctic Circumpolar Current (ACC) through vertical and horizontal turbulent mixing processes associated with mesoscale eddy activity. The path of the wind-driven ACC has long been known to be steered by deep seafloor topography [e.g., *Gordon and Baker*, 1986]. More recently, altimetric investigations have shown that eddy activity in the ACC is also modulated by bottom topography [*Sandwell and Zhang*, 1989, *Chelton et al.*, 1990; *Morrow et al.*, 1992; *Gille*, 1994]; sea surface variability is higher above the deeper basins (> 3 km) and much lower in the shallower areas (Figure 7). Thus both the path of ACC and the transient eddies associated with it are influenced by ocean depth.

Both observational and numerical studies of the influence of seafloor topography on ocean currents have been severely limited by the lack of accurate bathymetry; this is especially true in the Southern Ocean where areas as large as $2x10^5$ km^2 are unsurveyed. A striking example are three major ridges which lie directly in the paths of the ACC between 120˚W and 160˚W (Figure 3). The shallowest of the three features, first surveyed by a French Group [*Geli et al.,* 1997] in December of 1995, is a 400 km long ridge having a minimum depth of only 135 m. The other two topographic barriers are the 400 and 800 km long transverse ridges of the Udintsev and Eltanin Fracture Zones, respectively; both have a typical crest depth of less than 800 m while the surrounding seafloor is typically 3000 m deep and up to 6000 m deep in the fracture zone valleys.

In addition to the well known interaction of the mean ocean circulation with depth and the less well understood inverse correlation of mesoscale variability with depth, there have been recent suggestions that deep tidal mixing [*Polzin et al.,* 1997] and dissipation of ocean variability [*Yale et al.*, 1998] are enhanced over more rugged seafloor. Ocean floor roughness on scales less than 100 km is comprised of ubiquitous abyssal hill topography and less frequent, but higher amplitude, fracture zone topography. Bathymetric and altimetric studies [e.g., *Small,* 1994; *Smith* 1998] show a pronounced inverse correlation of seafloor roughness with increasing seafloor spreading rate. Seafloor generated at spreading rates lower than ~40 mm/a is characteristically rugged having rms amplitude of 100-200 m while seafloor generated at spreading rates greater than ~80 mm/a is always quite smooth having an rms amplitude of only 20-50 m. Preliminary results [*Yale et al.,* 1998] indicate that eddy kinetic energy (EKE) is greatest in the deeper ocean areas and over smooth seafloor. This anti-correlation between roughness and variability is strongest at higher latitudes suggesting a communication of the surface currents with the deep ocean floor. Rough bathymetry may transfer energy from the 100-300 length scales resolved by altimetry [Chapter 2] to smaller scales resulting in an apparent loss of EKE. Since numerical ocean models do not account for spatial variations in bottom friction and moreover, since they incorporate ad-hoc dissipation mechanisms, improvements in seafloor depth and roughness may lead to a better understanding of deep ocean mixing. The link between seafloor roughness and spreading rate provides an interesting possibility that vertical mixing of paleo-oceans depended on the average age of the ocean floor and thus the waxing and waning of the mantle convection patterns.

VII. PROSPECTS FOR THE FUTURE

While dense satellite altimeter measurements of the ocean surface have provided a fresh look at the ocean floor in the 20-100 km wavelength band, there are still many important problems in marine geology, physical oceanography, and marine biology where the current bathymetric model is inadequate. The question is, how can we improve our bathymetric models? Do we need to survey all of the oceans or are there more important target areas that could be used as calibration

points to address global problems? Would another non-repeat orbit altimeter mission provide a significant improvement?

Of course it is always possible to gather more ship soundings and the new multibeam systems can map swaths of seafloor that are 3 – 5 times the mean depth at 100 m horizontal resolution and 10 m vertical accuracy. Nevertheless, even with these new systems it will take more than 100 ship-years to completely map the ocean floor and the likelihood of obtaining funding for a complete mapping is extremely low. Thanks to the reconnaissance information provided by the ERS and Geosat altimeters during their geodetic missions, is it easier to justify cruises to remote areas and ship time can be spent on the most important targets. The process of complete seafloor mapping will probably not be accomplished in our lifetimes.

An important avenue for improving the bathymetric models, especially in the coastal areas where altimeter-derived bathymetry is unreliable, is to obtain dense surveys of exclusive economic zones that have been compiled by many countries. The difficult task is to assemble a list of available data and convert them to a common format (http://newport.pmel.noaa.gov/~kamphaus/time/data.html). Similarly, the US Navy and other Navies hold a wealth of data in classified archives that have the potential for revolutionizing bathymetric models [*Medea Report*, 1995]. These avenues are being explored by a number of groups, in particular, the engineers who model the potential for tsunami inundation of coastal areas.

Since bathymetric estimation in areas of sparse ship coverage is critically-dependent on the accuracy and resolution of the satellite-derived gravity an important question is: Can gravity field resolution and accuracy can be improved using more measurements or better processing? We feel there are two avenues for improvement. First, in the case of ERS data, better processing of the raw waveform data may lead to significant gains in accuracy but the improvement will be less than a factor of 2 [*Maus et al.*, 1998; *Laxon and McAdoo*, 1994]. Geosat and Topex altimeter data do not suffer from the noise problems of ERS onboard tracker and so we don't expect that retracking of the ERS data will provide a major improvement to the global gravity models. Second, in this chapter we discussed how ocean surface waves are the primary factor which limit the accuracy and resolution of the satellite-derived gravity. Since this is a random noise process, a factor of 2 improvement will require 4 times more data. ERS and Geosat data span 2.5 years in the geodetic mode, so another 5 years of altimetry in a non-repeat mission would provide dramatic improvement.

VIII. APPENDIX – Interaction of the radar pulse with the rough ocean surface

A. *Beam-limited footprint*

The main advantages of operating an altimeter in the microwave part of the spectrum (~13GHz) are that the atmosphere is very transparent and there is little stray radiation coming from the Earth.

The main limitation is that the illumination pattern on the surface of the ocean is very broad for reasonable sized antennas. Consider an antenna of diameter D_a, at an mean altitude H operating at a wavelength of λ.

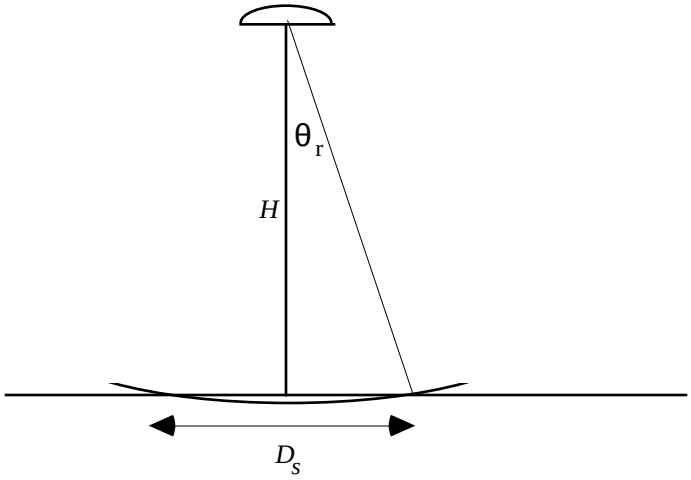

The angular resolution θ_r of a circular aperture having radius D_a is given by

$\sin \theta_r = 1.22 \frac{\lambda}{D_a}$. Therefore the diameter of the illumination pattern on the ocean surface is

(16)

$$D_s = 2H \sin\theta_r = 2.44 H \frac{\lambda}{D_a}$$

This illumination diameter is called the *beam width* of the radar. It is typically quite large (D_s = 43 km when D_a = 1 m, λ = 22 mm, H = 800 km altitude). Using this configuration, it will be impossible to achieve the 16 km wavelength horizontal resolution required for gravity field recovery and bathymetric estimation. However, one benefit of this wide illumination pattern is that small (~1 degree) pointing errors away from *nadir* have an insignificant effect on the range measurement.

To achieve the 20 mm range precision described in the previous Chapters of the book, for example, one must measure the travel time of the radar echo to an accuracy of $\Delta t = 2\Delta h/c = 1.3 \times 10^{-10}$ s. This can be translated into the bandwidth of the radiation needed to form a sharp pulse $\Delta\nu = 1/\Delta t$. In this case an 8 GHz bandwidth is needed. Note that the carrier frequency of our radar altimeter is 13 GHz so the pulse must span most of the electromagnetic

spectrum. Obviously one can't use the entire EM spectrum; in practice one is restricted to a bandwidth of only 0.3 GHz. However, it turns out that ocean waves effectively limit the accuracy of the travel time measurement so a high bandwidth is unnecessary; the desired range resolution can only be achieved by averaging thousands of pulses with the hope that they are randomly distributed around the correct mean value.

B. *Pulse-limited footprint*

Assume for the moment that the ocean surface is perfectly flat (actually ellipsoidal) but has point scatters to reflect the energy back to the antenna. The radar forms a sharp pulse having a length of about 3 nanoseconds corresponding to the 0.3 GHz bandwidth. In practice, to reduce the peak output requirement of the transmitter, the radar emits a long-duration, frequency-modulated chirp. The chirped radar signal reflects from the ocean surface and returns to the antenna where it is convolved with a *matched filter* to regenerate the desired pulse. This is a common signal processing approach used in all radar systems. After the matched filter one can treat the measurement as a pulse. The diagram below illustrates how the pulse interacts with a flat sea surface.

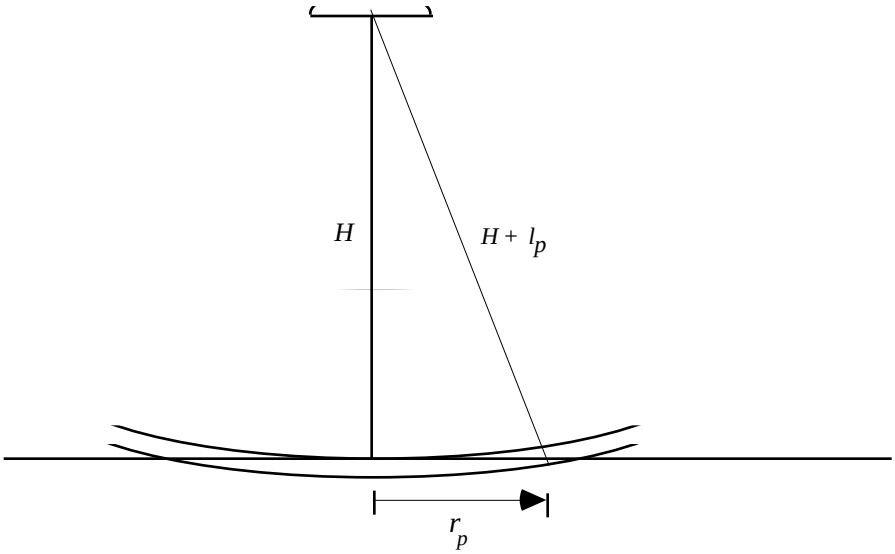

where

H	-	satellite altitude	800 km
t_p	-	pulse length	3×10^{-9} s
c	-	speed of light	3×10^{8} m/s
$l_p = c\, t_p$	-	length of pulse	1 m
r_p	-	radius of pulse on ocean surface	

The radius of the leading edge of the pulse is derived as follows.

(17)

$$H^2 + r_p^2 = \left(H + l_p\right)^2 = H^2 + l_p^2 + 2Hl_p$$

The H^2 cancels and we can assume l_p^2 is very small compared with the other terms so the pulse radius is

(18)

$$r_p = \sqrt{2Hl_p} = \sqrt{2Hct_p}$$

For a 3 ns pulse length the pulse radius is 1.2 km so the diameter or *footprint* of the radar is 2.4 km. Since this footprint is much less than the beam width, the power that is returned to the radar will be a ramp function.

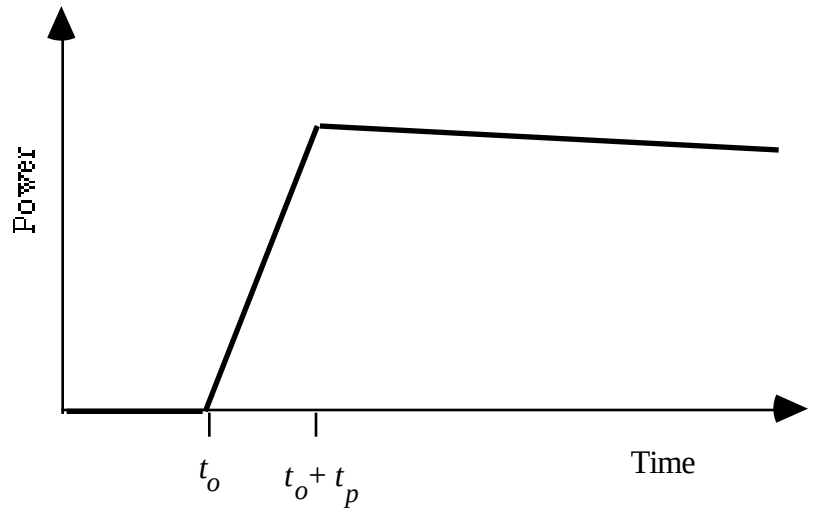

The power begins to ramp-up at time $t_o = 2H/c$ and the ramp extends for the duration of the pulse. At times greater than $t_o + t_p$, the diameter of the radar pulse continues to grow and energy continues to return to the radar. The amplitude of this energy decreases gradually according to the illumination pattern of the radar on the ocean surface. Because of the finite pulse width, the bottom and top of the ramp will be rounded.

C. *Significant wave height*

Of course the actual ocean surface has roughness due to ocean waves and swell. This ramp-like return power will be convolved with the height distribution of the waves within the footprint to

further smooth the return pulse and make the estimate of the arrival time of the leading edge of the pulse less certain [*Walsh et al.,* 1978]. We can investigate the effects of wave height on both return pulse length and footprint diameter using a Gaussian model for the height distribution of ocean waves. This model provides and excellent match to observed wave height [*Stewart, 1985*].

(19)

$$G(h) = \frac{1}{\sqrt{2\pi}\Delta h} \exp\left(-\frac{h^2}{2\Delta h^2}\right)$$

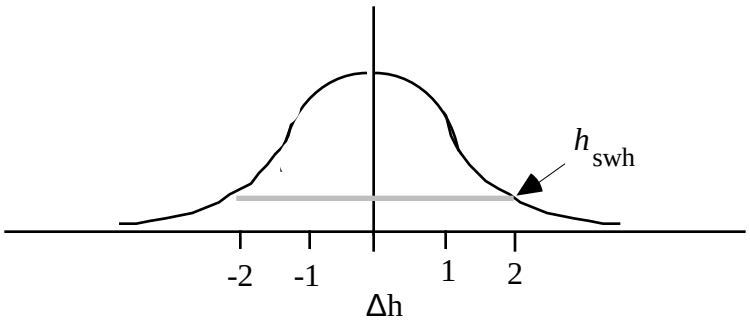

An observer on a ship can accurately report the peak-to-trough amplitude of the highest waves; this is called the significant wave height and it is $h_{swh} = 4\Delta h$. Because the altimeter footprint is broad compared with the wavelength of the swell, this waveheight distribution is convolved with the radar pulse. The amplitude of the return pulse A will be a Gaussian function of two-way travel time difference $\tau = 2H/c$.

(20)

$$A(\tau) = \exp\left(-\frac{2c^2\tau^2}{h_{swh}^2}\right)$$

The broadening of the radar return pulse t_w is measured as the full width of the pulse where the power is 1/2.

(21)

$$\frac{1}{2} = \exp\left(-\frac{c^2 t_w^2}{h_{swh}^2}\right) \quad so \quad t_w^2 = \frac{h_{swh}^2}{c^2}\ln 2.$$

Since we were unable to form a very sharp radar pulse because the radar bandwidth is limited to 0.3 GHz, the total width of the return pulse will be established by convolving the outgoing pulse with the Gaussian wave model. If the outgoing pulse can also be modeled by a Gaussian function having a pulse width of t_p, then the total width of the return pulse is given by

(22)

$$t^2 = t_p^2 + \frac{h_{swh}^2}{c^2} \ln 2.$$

This provides and expression for the pulse width as a function of significant wave height (SWH). Similarly the diameter of the pulse as a function of significant wave height is

(23)

$$d = 2\sqrt{(2cHt)} \ .$$

Both functions are shown in Figure 8 for SWH ranging from 1 to 10 m. It is clear that the quality of the altimeter measurement will decrease with increasing SWH. In practice we have found that Geosat, ERS, and Topex data are unreliable when SWH exceeds about 6 m.

Significant Wave height is typically 2 meters so the radar footprint is typically 3.5 km and the pulse-length increases from 1 m to 2 m. Now we see that our original plan of having a very narrow pulse of 60 ps to resolve 20 mm height variations was doomed because the ocean surface is usually rough; a 3 ns (1 m) pulse is all that could be resolved anyway. In addition is clear that the wavelength resolution of the sea surface height recovery will typically be worse than 7 km. Given this poor inherent range accuracy of 1-2 m, how do we achieve the 20 mm resolution needed for our applications? The way to improve the accuracy by a factor of 10^2 is to average 10^4 measurements and hope the noise is completely random.

The speed of light provides an interesting limitation for space-borne ranging systems. At a typical orbital altitude of 800 km it takes 5.2 milliseconds for the pulse to complete its round trip route. One can have several pulses en-route but because we actually send a long chirp rather than a pulse, the pulse repetition frequency is limited to about 1000 pulses per second; during one second, the altimeter moves about 7000 m along its track. Thus in each second there are 1000 pulses available for averaging; this will reduce the noise from 1.5 m to 0.05 m. Further averaging can be done for many of the oceanographic applications where the horizontal length scale of the feature is > 50 km. Of course one should be careful to remove all of the sharp geoid signals using

the full resolution data [Chapter 10, Figure 3] and then smooth the residual data along the profile to achieve higher accuracy. Typically the data are delivered as a geophysical data record (GDR) where 1000 pulses are averaged and then decimated to 1 Hz. This boxcar filter followed by decimation folds the shorter wavelength noise back to longer wavelengths and further decreases the accuracy and horizontal resolution of the data. Data at 10Hz sampling are also provided with the GDR and we recommend that the user design a convolution filter to achieve the desired spectral output. Our gravity fields and estimated bathymetry are produced with such filters.

D. *Modeling the return waveform*

There are several engineering issues related to picking the travel time of the return pulse [*Hayne et al*., 1994; *Rodriguez and Martin*, 1994]. First, after the return echo is passed through a matched filter to form the pulse, the pulse power is recorded at 64 times in a window that is about 30 ns (~10 m) long. An adaptive tracker is used to keep the power ramp in the center of the window. The ocean surface is typically smooth at length scales greater than the footprint so keeping the pulse in the window is not a problem. However, over land or ice, it is not usually possible to keep the pulse within the window because 10 m variations in topography over several kilometers of horizontal distance are quite common. The Geosat altimeter loses lock over land and must re-acquire the echo soon after moving back over the ocean. The ERS-1/2 altimeters widen the gate spacing over land and ice so they can measure land topography as well as ocean topography.

After recording the waveform of the return pulse, 100 echoes are averaged and an analytic function is fit to each waveform [*Maus et al.,* 1998]. The function has 3 parameters: 1) the position of the steepest part of the ramp provides the range estimate; 2) the width of the ramp provides and estimate of SWH; 3) and the height of the ramp (called sigma-naught σ_o) provides an estimate of surface roughness at the 20-30 mm length scale. This latter measurement can be related to surface wind speed since wind will roughen the ocean surface. Precise calibration is performed for each of the three measurements. Absolute range calibration is, for example, performed in the open ocean using an oil platform having a GPS receiver and accurate tide gauge [*Christensen et al.*, 1994]. Both SWH and wind speed are calibrated using open-ocean shipboard measurements.

REFERENCES

Banks, R. J., Parker, R. L., and Huestis, S. P. (1977). Isostatic compensation on a continental scale: Local versus regional mechanisms. *Geophys. J. R. astr. Soc*. **51**, 431-452.

Baudry, N., and Calmant, S. (1991). 3-D Modeling of seamount topography from satellite altimetry. *Geophys. Res. Lett*. **18**, 1143-1146.

Bettadpur, S. V., and R. J. Eanes, R. J. (1994). Geographical representation of radial orbit perturbations due to ocean tides: Implications for satellite altimetry. *J. Geophys. Res*. **99**, 24,883-24,898.

Calmant, S. (1994). Seamount topography of least-squares inversion of altimetric geoid heights and shipborne profiles of bathymetry and/or gravity anomalies. *Geophys. J. Int*. **119**, 428-452.

Canadian Hydrographic Service (1981). General bathymetric Chart of the Oceans (GEBCO). Hydrographic Chart Distribution Office, Ottawa, Canada.

Cazenave, A., Schaeffer, P., Berge, M., and Brossier, C. (1996). High-resolution mean sea surface computed with altimeter data of ERS-1 (Geodetic Mission) and TOPEX-POSEIDON. *Geophys. J. Int*. **125**, 696-704.

Chelton, D. B., Schlax, M. G., Witter, D. L., and Richman, J. G. (1990). Geosat altimeter observations of the surface circulation of the Southern Ocean. *J. Geophys. Res*. **95**, 17,877-17,903.

Christensen, et al. (1994). Calibration of TOPEX/POSEIDON at Platform Harvest. *J. Geophys. Res*. **99**, 24,465-24,486.

Devey, C., et al. (1997). The Foundation Seamount Chain: A first survey and sampling. *Mar. Geol.* **137**, 191-200.

Dixon, T. H., Naraghi, M., McNutt, M. K., and Smith, S. M. (1983). Bathymetric prediction from Seasat altimeter data. *J. Geophys. Res*. **88**, 1563-1571.

Geli. L. et al., (1997). Evolution of the Pacific-Antarctic Ridge south of the Udintsev Fracture Zone, *Science,* **278,** 1281-1284.

Gille, S. T. (1994). Mean sea surface height of the Antarctic circumpolar current from Geosat data: Method and application. *J. Geophys. Res*. **99**, 18,255-18,273.

Gordon, A. L., and Baker, T. N. (1986). "Southern Ocean Atlas." Published for the International Decade of Ocean Exploration, National Science Foundation.

Haxby, W. F., Karner, G. D., LaBrecque, J. L., and Weissel, J. K. (1983). Digital images of combined oceanic and continental data sets and their use in tectonic studies. *EOS Trans. Amer. Geophys. Un*. **64**, 995-1004.

Hayne, G. S., Hancock, D. W., Purdy, C. L., and Callahan, P. S. (1994). The corrections for significant wave height and altitude effects in the TOPEX radar altimeter. *J. Geophys. Res*. **99**, 24,941-24,955.

Heiskanen, W. A., and H. Moritz, H. (1967). "Physical Geodesy." W. H. Freeman and Co., San Francisco.

Hwang, C., Kao, E.-C., and Parsons, B. (1998). Global derivation of marine gravity anomalies from Seasat, Geosat, ERS-1 and TOPEX/POSEIDON altimeter data. *Geophys. J. Int*. 134, 449-459.

Hwang, C., and Parsons, B. (1996). An optimal procedure for deriving marine gravity from multi-satellite altimetry. *J. Geophys. Int*. 125, 705-719.

Imel, D.A. (1994). Evaluation of the TOPEX/POSEIDON dual-frequency ionospher correction. *J. Geophys. Res*. **99**, 24,895-24,906.

Jung, W. Y., and Vogt, P. R. (1992). Predicting bathymetry from Geosat-ERM and shipborne profiles in the South Atlantic ocean. *Tectonophysics* **210**, 235-253.

Laxon, S., and McAdoo, D. (1994). Arctic ocean gravity field derived from ERS-1 satellite altimetry. *Science* **265**, 621-624.

Lemoine, F. G., et al. (1998). The development of the joint NASA CSFC and the national Imagery and Mapping Agency (NIMA) geopotential model EGM96. Goddard Space Flight Center, NASA, NASA/TP-1998-206861.

Liu, C.-S., Sandwell, D. T., and J. R. Curray, J. R. (1982). The negative gravity field over the 85˚ Ridge. *J. Geophys. Res*., **87**, 7673-7686.

Maia, M., et al. (1999). The Foundation Seamounts: A ridge-hotspot interaction in the South Pacific. Preprint.

Mammerickx, J. (1992). The Foundation Seamounts: tectonic setting of a newly discovered seamount chain in the South Pacific. *Earth Planet. Sci. Lett.* **113**, 293-306.

Marks, K. M. (1996). Resolution of the Scripps/NOAA marine gravity field from satellite altimetry. *Geophys. Res. Lett*. **23**, 2069-2072.

Maus, S., Green, C. M., and Fairhead, J. D. (1998). Improved ocean-geoid resolution from retracked ERS-1 satellite altimeter waveforms. *Geophys. J. Int*. **134**, 243-253.

McKenzie, D. P. (1976). Some remarks on heat flow and gravity anomalies. *J. Geophys. Res*. **72**, 6261-6273.

McKenzie, D. P., and Bowin, C. (1976). The relationship between bathymetry and gravity in the Atlantic Ocean. *J. Geophys*. Res. **81**, 1903-1915.

McNutt, M. (1979). Compensation of oceanic topography: An application of the response function technique to the Surveyor area. *J. Geophys. Res*. **84**, 7589-7598.

Medea, Scientific Utility of Naval Environmental Data. MEDEA Office, 1995.

Menard, H. W., and Smith, S. M. (1966). Hypsometry of Ocean Basin Provinces. *J. Geophys. Res*. **71**, 4305-4325.

Morrow, R., Church, J., Coleman, R., Chelton, D., and N. White, N. (1992). Eddy momentum flux and its contribution to the Southern Ocean momentum balance. *Nature* **357**, 482-484.

Mueller, R. D., Roest, W. R., Royer, J.-Y., Gahagan, L. M., and Sclater, J. G. (1997). Digital isochrons of the world's ocean floor. *J. Geophys. Res*. **102**, 3211-3214.

Nettleton, L. L. (1939). Determination of Density for Reduction of Gravity Observations. *Geophysics* **4**, 176-183.

Noreus, J. P. (1995). Improved resolution of Geosat altimetry using dense sampling and polynomial adjusted averaging. *Int. J. Remote Sensing* **16**, 2843-2862.

Parker, R. L. (1973). The rapid calculation of potential anomalies. *Geophys. J. R. astr. Soc*. **31**, 447-455.

Parker, R. L. (1994). "Geophysical Inverse Theory." Princeton University Press, Princeton.

Parsons, B. (1982). Causes and consequences of the relation between area and age of the ocean floor. *J. Geophys. Res*. **87**, 289-302.

Parsons, B., and Sclater, J. G. (1977). An analysis of the variation of the ocean floor bathymetry and heat flow with age. *J. Geophys. Res*. **82**, 803-827.

Polzin, K. L., Toole, J. M., Ledwell, J. R., and Schmitt, R. W. (1997). Spatial variability of turbulent mixing in the abyssal ocean. *Science* **276**, 93-96.

Ramillien, G., and Cazenave, A. (1997). Global bathymetry derived from altimeter data of the ERS-1 Geodetic Mission. *J. Geodynamics* **23**, 129-149.

Rapp, R. H., and Yi, Y. (1997). Role of ocean variability and dynamic topography in the recovery of the mean sea surface and gravity anomalies from satellite altimeter data. *J. Geodesy* **71**, 617-629.

Ribe, N. M. (1982). On the interpretation of frequency response functions for oceanic gravity and bathymetry. *Geophys. J. R. Astron. Soc*. **70**, 273-294.

Rodriguez, E., and Martin, J. M. (1994). Assessment of the TOPEX altimeter performance using waveform retracking. *J. Geophys. Res*. **99**, 24,957-24,969.

Sandwell, D. T. (1984a). A detailed view of the South Pacific from satellite altimetry. *J. Geophys. Res*. **89**, 1089-1104.

Sandwell, D. T. (1991). Geophysical applications of satellite altimetry. *Rev. Geophys. Suppl*. **29**, 132-137.

Sandwell, D. T. (1992). Antarctic marine gravity field from high-density satellite altimetry. *Geophys. J. Int*. **109**, 437-448.

Sandwell, D. T., and Smith, W. H. F. (1997). Marine gravity anomaly from Geosat and ERS-1 satellite altimetry. *J. Geophys. Res*. **102**, 10,039-10,054.

Sandwell, D. T., and Zhang, B. (1989). Global mesoscale variability from the Geosat exact repeat mission: Correlation with ocean depth. *J. Geophys. Res*. **94**, 17,971-17,984.

Sichoix, L., and Bonneville, A. (1996). Prediction of bathymetry in French Polynesia constrained by shipboard data. *Geophys. Res. Lett.*, **23**, 2469-2472.

Small, C. (1994). A global analysis of mid-ocean ridge axial topography. *Geophys. J. Int*. **116**, 64-84.

Smith, W. H. F. (1993). On the accuracy of digital bathymetry data. *J. Geophys. Res*. **98**, 9591-9603.

Smith, W. H. F. (1998). Seafloor tectonic fabric from satellite altimetry. *Ann. Rev. Earth Planet. Sci*. **26**, 697-738.

Smith, W. H. F., and Sandwell, D. T. (1994). Bathymetric prediction from dense satellite altimetry and sparse shipboard bathymetry. *J. Geophys. Res*. **99**, 21,803-21,824.

Smith, W. H. F., and Sandwell, D. T. (1997). Global sea floor topography from satellite altimetry and ship depth soundings. *Science* **277**, 1956-1961.

Smith, W. H. F., and Wessel, P. (1990). Gridding with continuous curvature splines in tension. *Geophysics* **55**, 293-305.

Stewart, R. H. (1985) "Methods of Satellite Oceanography." University of California Press, Berkeley.

Tapley, B. D., Chambers, D. P., Shum, C. K., Eanes, R. J., Ries, J. C., and Stewart, R. H. (1994). Accuracy assessment of large-scale dynamic ocean topography from Topex/Poseidon altimetry. *J. Geophys. Res*. **99**, 24,605-24,617.

Walsh, E. J., Uliana, E. A., and Yaplee, B. S. (1978). Ocean wave height measured by a high resolution pulse-limited radar altimeter. *Boundary-Layer Meterology* **13**, 263-276.

Watts, A. B. (1978). An analysis of isostasy in the world's oceans: 1, Hawaiian-Emperor seamount chain. *J. Geophys. Res*. **83**, 5989-6004.

Watts, A. B. (1979). On geoid heights derived from Geos-3 altimeter data and flexure of the lithosphere along the Hawaiian-Emperor seamount chain. *J. Geophys. Res*. **38**, 119-141.

Wessel, P. (1992). Thermal stress and the bimodal distribution of elastic thickness estimates of the oceanic lithosphere, *J. Geophys. Res.*, **97**, 14177-14193.

Wessel, P., and Smith, W. H. F. (1991). Free software helps map and display data. *EOS Trans. AGU* **72**, 445-446.

Wessel, P., and Smith, W. H. F. (1996). A global, self-consistent, hierarchical, high-resolution shoreline database. *J. Geophys. Res*. **101**, 8741-8743.

Wessel, P., and A. B. Watts, A. B. (1988). On the accuracy of marine gravity measurements. *J. Geophys. Res*. **93**, 393-413.

Yale, M. M. (1997). Modeling Upper mantle Rheology with Numerical Experiments and Mapping Marine Gravity with Satellite Altimetry. Ph.D. Thesis, University of Calififormia, San Diego.

Yale, M. M., Gille, S. T., and Sandwell, D. T. (1998). Ocean mixing- mesoscale EKE, bathymetry, and seafloor roughness seen by ERS-1/2 and Topex. *EOS Trans. AGU* **79**, F213.

Yale, M. M., Sandwell, D. T., and Smith, W. H. F. (1995). Comparison of along-track resolution of stacked Geosat, ERS-1 and TOPEX satellite altimeters. *J. Geophys. Res*. **100**, 15,117-15,127.

Figure 1. Fundamental limitations of topographic recovery from gravity anomaly measurements are illustrated by seamounts (left) and plateau (right). The gravity signatures of the closely-spaced seamounts (4 km apart and 1 km tall) are strong and distinct when the average ocean depth is 2 km or less but their signatures combine and become weak when the ocean depth is 4 km. The isostatically compensated step in depth produces a local gravitational edge effect that is strongly attenuated at a distance of 150 km from the step; thus the gravity far from the step does not provide information on the overall depth offset across the step.

Figure. 2. (upper) Gravity/topography ratio versus wavelength for uncompensated topography (solid curve) and elastic plate flexure models (dashed - 30 km thickness, dotted - 5 km thickness). Gravity/topography ratio is highly variable in the *compensation band* but uniform over the *prediction band* and *unresolved band.*
(lower) Topography/gravity ratio for same three models illustrates the fundamental limitations of predicting topography from gravity. Errors in the satellite-derived gravity anomaly are typically 4 mGal so when the topography/gravity ratio exceeds 50 m/mGal, the predicted noise of 200 m will exceed the typical seafloor roughness. Sparse ship soundings can be used to constrain longer wavelengths while multibeam bathymetry is needed to constrain shorter wavelengths.

Figure. 3. (a) Tracks of stacked Geosat/ERM (17-day repeat cycle), Geosat/GM, ERS-1 Geodetic Phase (168-day repeat cycle) and stacked ERS-1 (35-day repeat).
(b) Ship tracks in area of the Eltanin and Udintsev transform faults. Track density is sparse except along the Pacific-Antarctic plate boundary.
(c) Gravity anomaly (mGal) derived from all 4 altimeter data sets.
(d) Bathymetry (m) estimated from ship soundings and gravity inversion. Red curves mark the sub-Antarctic and polar fronts of the Antarctic Circumpolar Current [*Gille,* 1994]. The Sub-Antarctic Front (SAF-red) passes directly over a NW-trending ridge having a minimum ocean depth of 135 m. The Polar Front (PF) is centered on the 6000m deep valley of the Udintsev transform fault.

Figure. 4. Global map of predicted seafloor depth [*Smith and Sandwell,* 1997] and elevation from GTOPO-30.

Figure. 5. (a) 3-D perspective plot of the Foundation seamount chain and ship track used as a blind test of our bathymetric prediction V6.2.

(b) Comparison of measured depth along ship track (middle) with ETOPO-5 (upper) and our predicted depth (lower). These ship data were acquired after the V6.2 of the bathymetric grid was completed.

Figure. 6. Hypsometric curves of the ocean basins based on pre-1977 ship soundings (upper light shading) and ETOPO-5 (upper black) and our new bathymetric prediction V6.2 (lower). Note that the new solution has two peaks in the hypsometry at 5100 m and 4200 m depth.

Figure 7. rms variability of sea surface slope derived from 116 repeat cycles of Topex altimetry (10-day repeat), 16 cycles of ERS-1 altimetry (35-day repeat), and 62 cycles of Geosat altimetry (17-day repeat). Black contours (1 km interval) are based on predicted depth [*Smith and Sandwell,* 1997]. White curves mark the sub-Antarctic front and polar front estimated from Geosat altimetry using a meandering jet model [*Gille,* 1994]. Slope variability is related to both the meandering of the fronts and the variations in ocean depth. The combination of altimeter profiles from T/P, ERS-1, and ERS-2 may provide complete spatial and temporal resolution of high-latitude eddies.

Figure 8. (lower) return pulse length in meters as a function of significant wave height. (upper) diameter of the radar pulse on the ocean surface as a function of significant wave height. A typical significant wave height of 2 m is marked by a large gray dot.

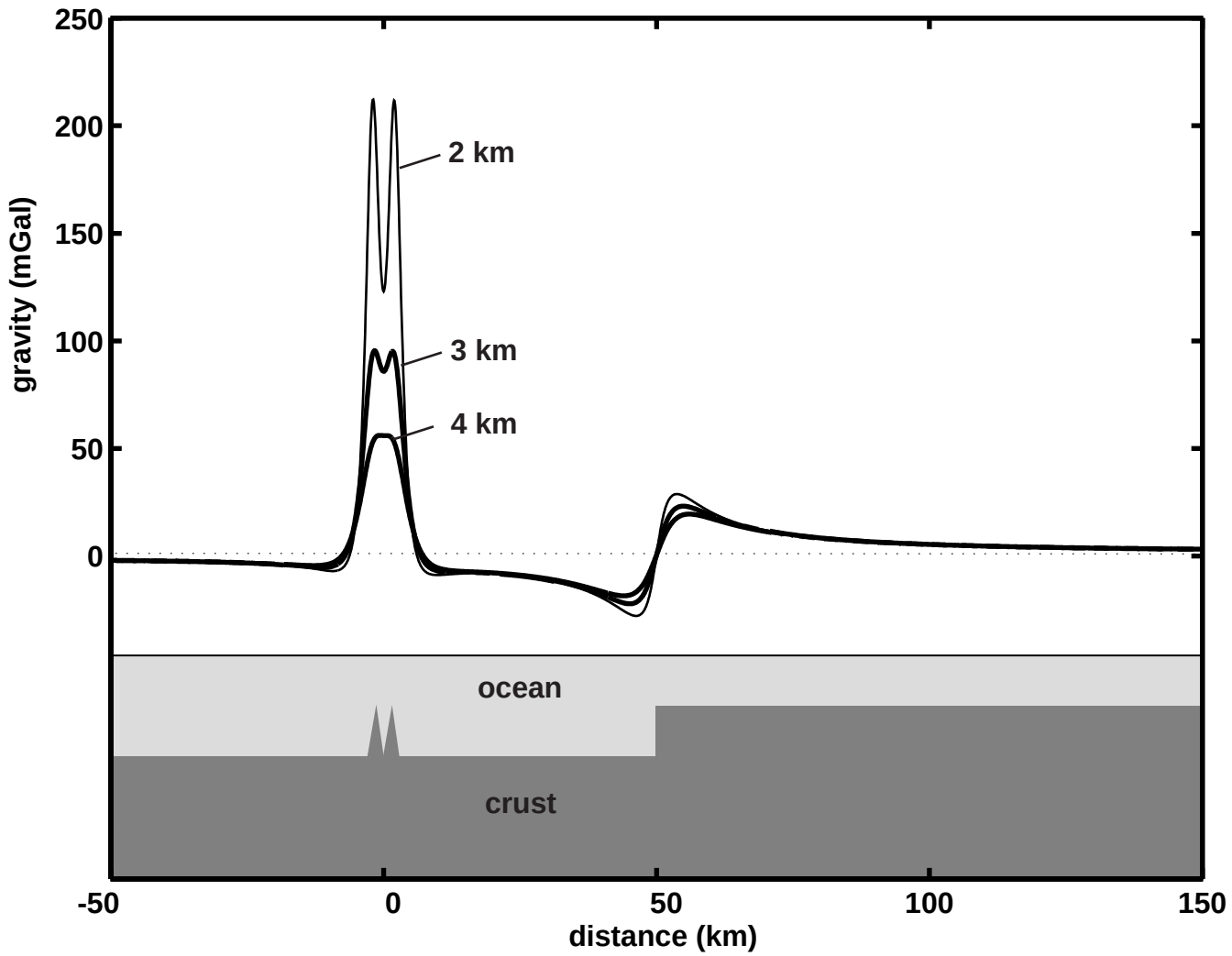
250
200
150
100
50
0
gravity (mGal)
2 km
3 km
4 km
ocean
crust
-50
0
50
100
150
distance (km)

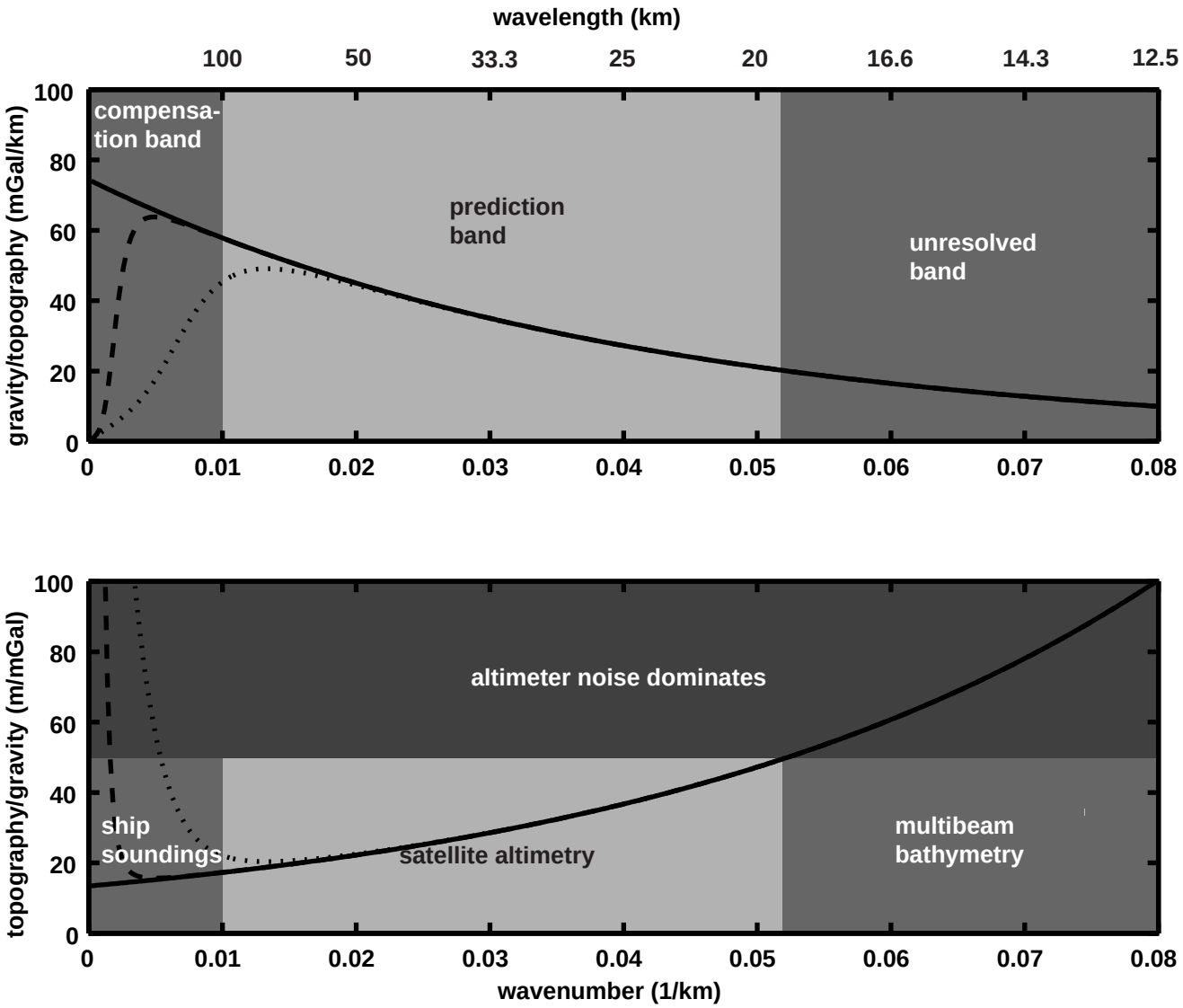
wavelength (km)
100
50
33.3
25
20
16.6
14.3
12.5
gravity/topography (mGal/km)
compensa-
tion band
prediction
band
unresolved
band
0
20
40
60
80
100
0
0.01
0.02
0.03
0.04
0.05
0.06
0.07
0.08
topography/gravity (m/mGal)
altimeter noise dominates
ship
soundings
satellite altimetry
multibeam
bathymetry
wavenumber (1/km)

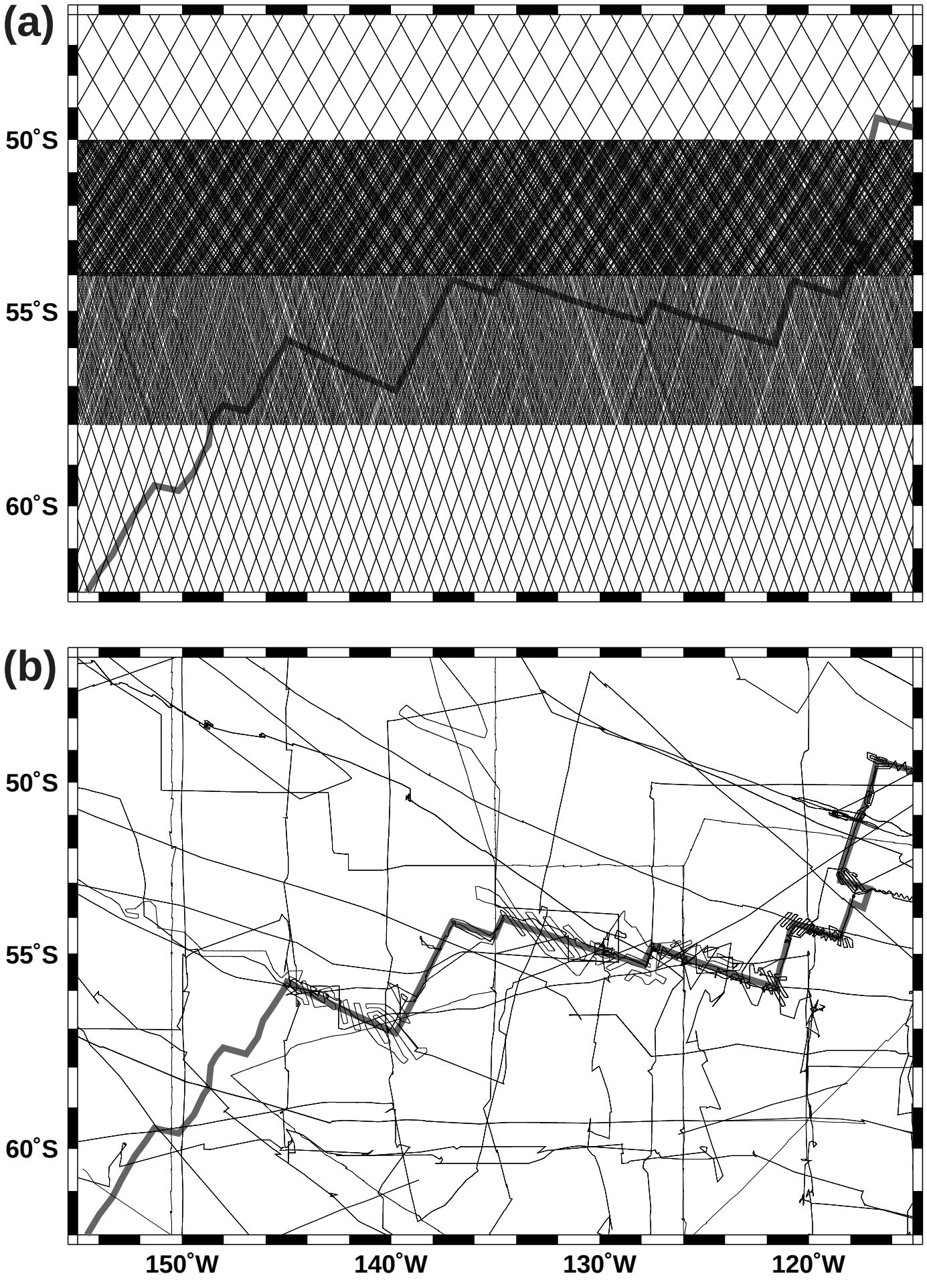
(a)
50˚S
55˚S
60˚S
(b)
50˚S
55˚S
60˚S
150˚W
140˚W
130˚W
120˚W

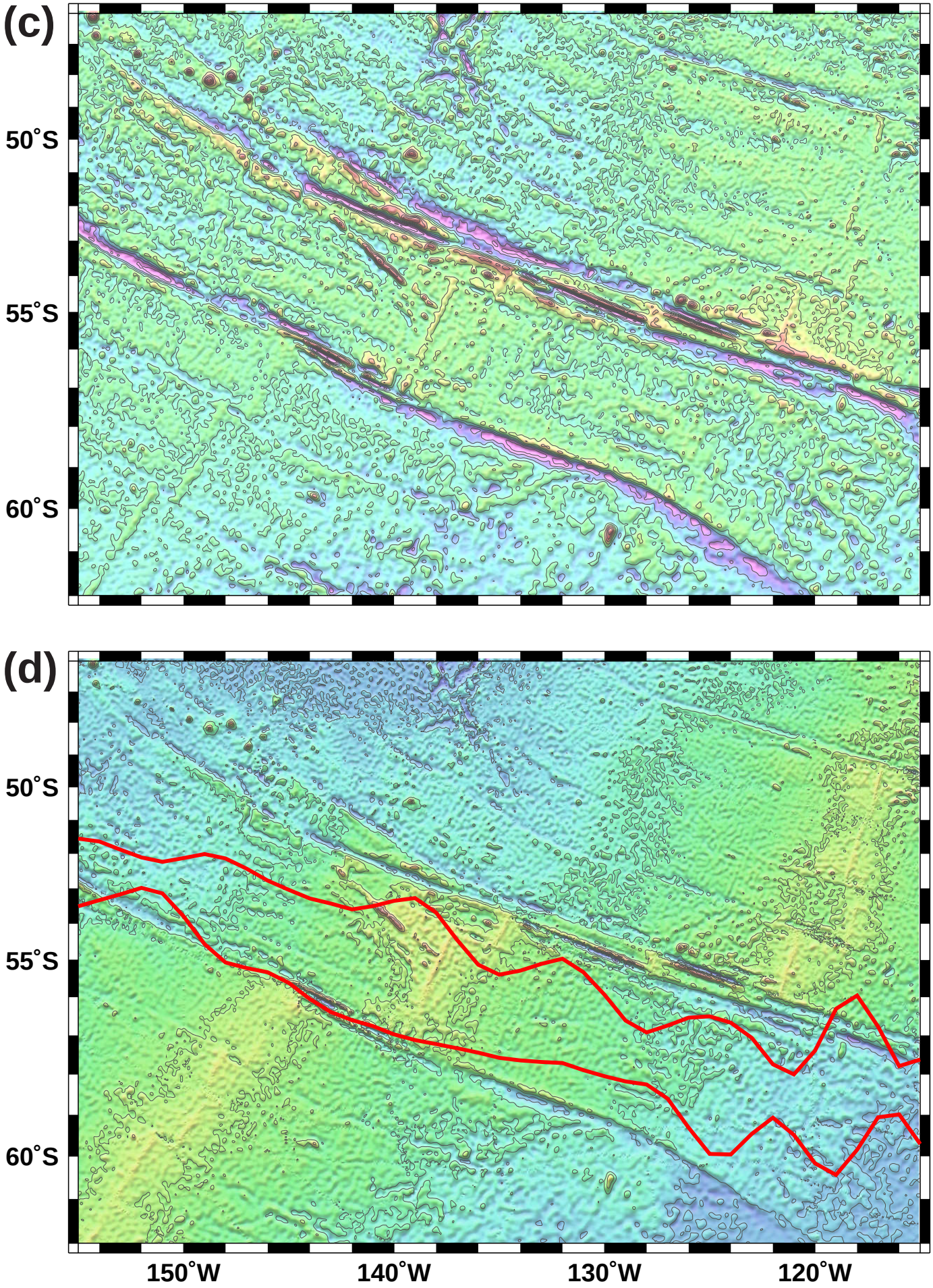
(c)
50˚S
55˚S
60˚S
(d)
50˚S
55˚S
60˚S
150˚W
140˚W
130˚W
120˚W

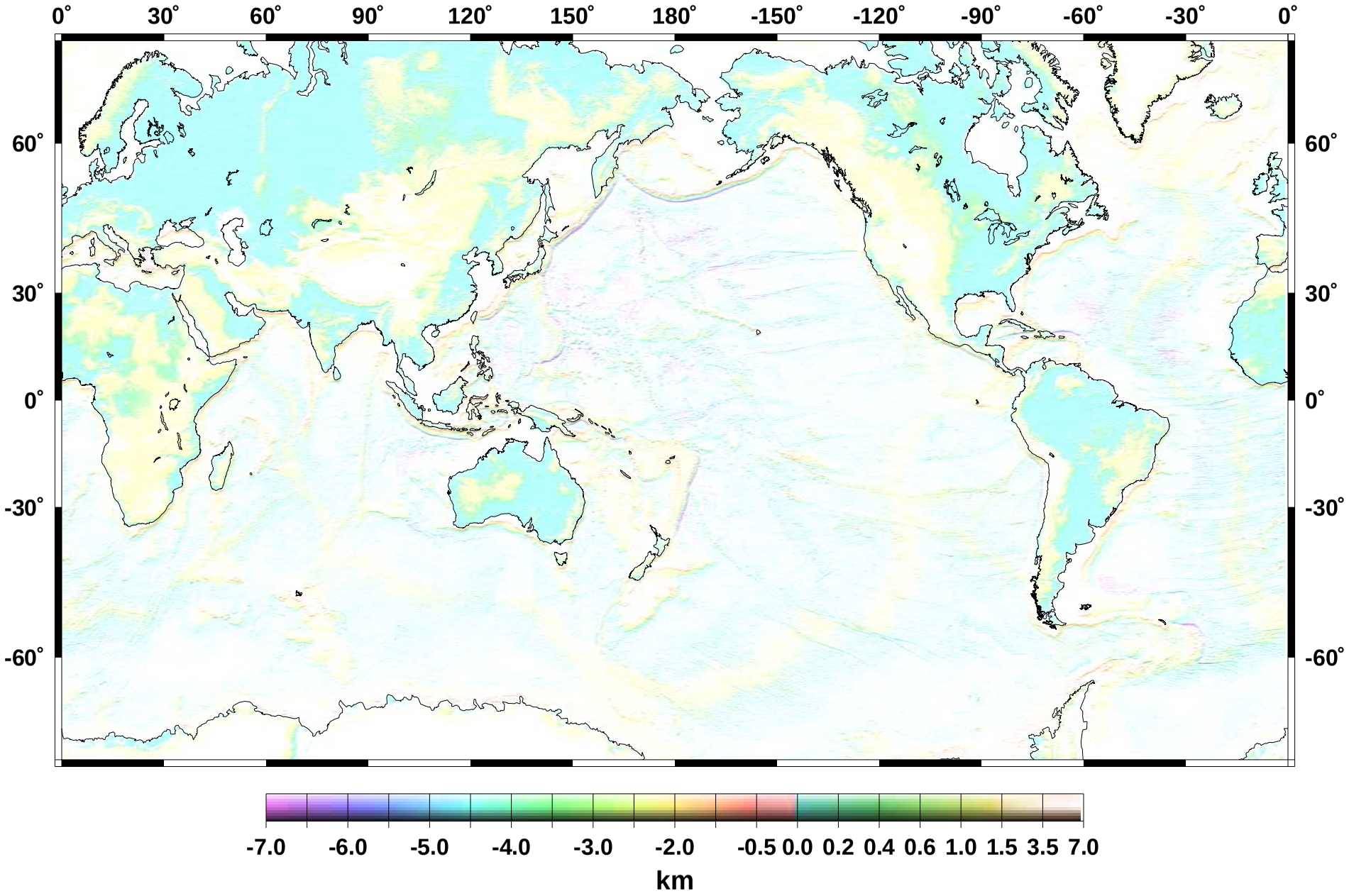
0°
30°
60°
90°
120°
150°
180°
-150°
-120°
-90°
-60°
-30°
0°
60°
30°
0°
-30°
-60°
-7.0
-6.0
-5.0
-4.0
-3.0
-2.0
-0.5
0.0
0.2
0.4
0.6
1.0
1.5
3.5
7.0
km

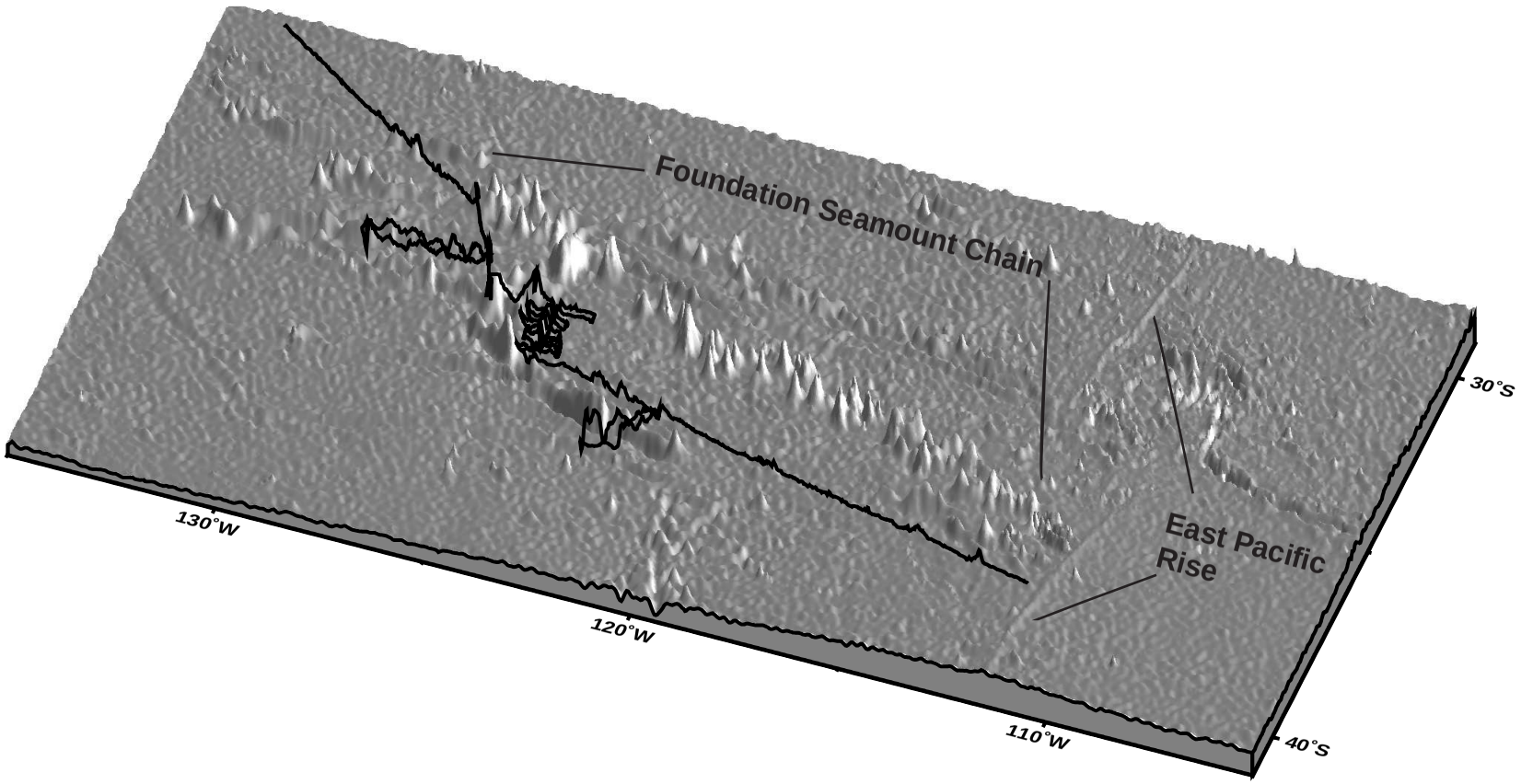
Foundation Seamount Chain
East Pacific Rise
130°W
120°W
110°W
30°S
40°S

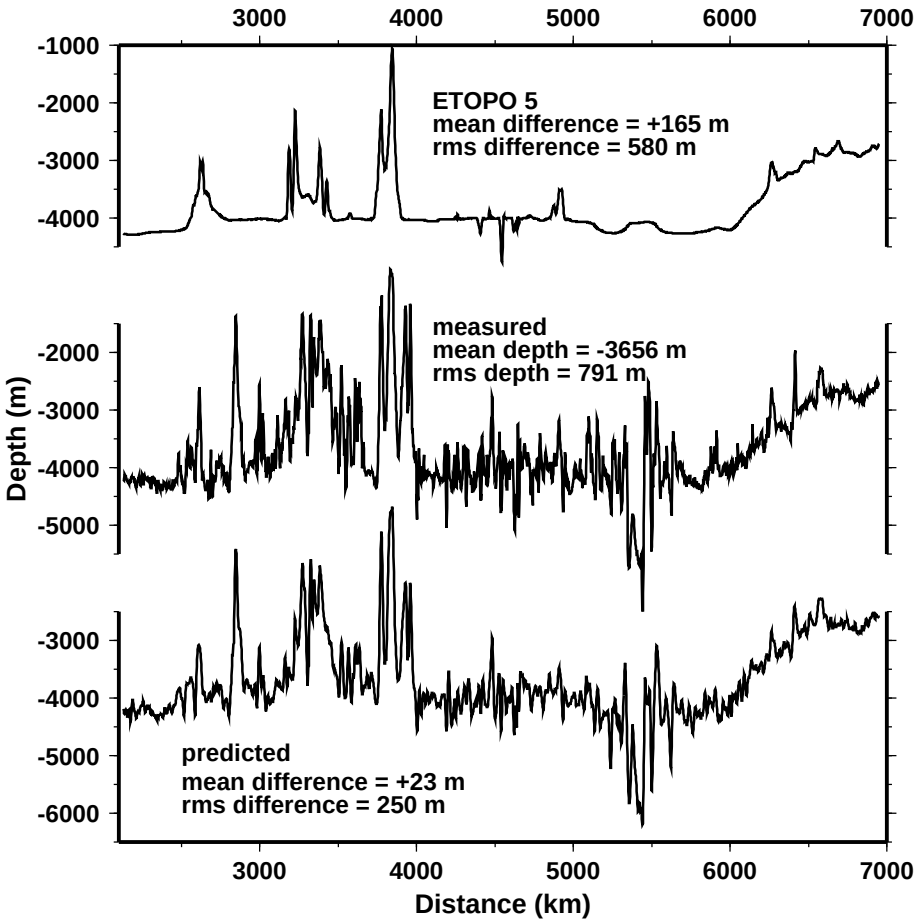
3000
4000
5000
6000
7000
-1000
-2000
-3000
-4000
ETOPO 5
mean difference = +165 m
rms difference = 580 m
-2000
-3000
-4000
-5000
measured
mean depth = -3656 m
rms depth = 791 m
Depth (m)
-3000
-4000
-5000
-6000
predicted
mean difference = +23 m
rms difference = 250 m
3000
4000
5000
6000
7000
Distance (km)

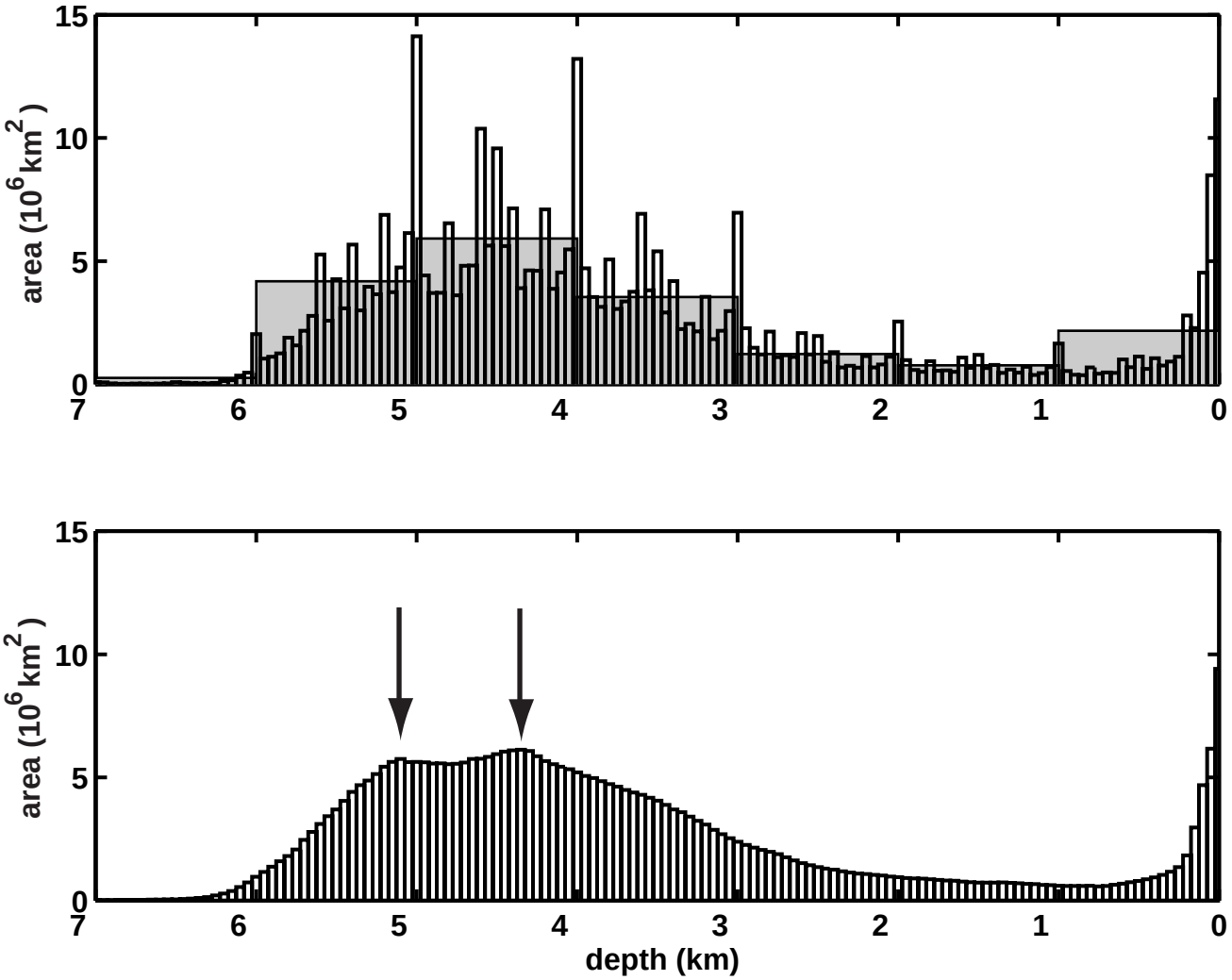
15
10
5
0
area (10^6 km^2)
7
6
5
4
3
2
1
0
15
10
5
0
area (10^6 km^2)
7
6
5
4
3
2
1
0
depth (km)

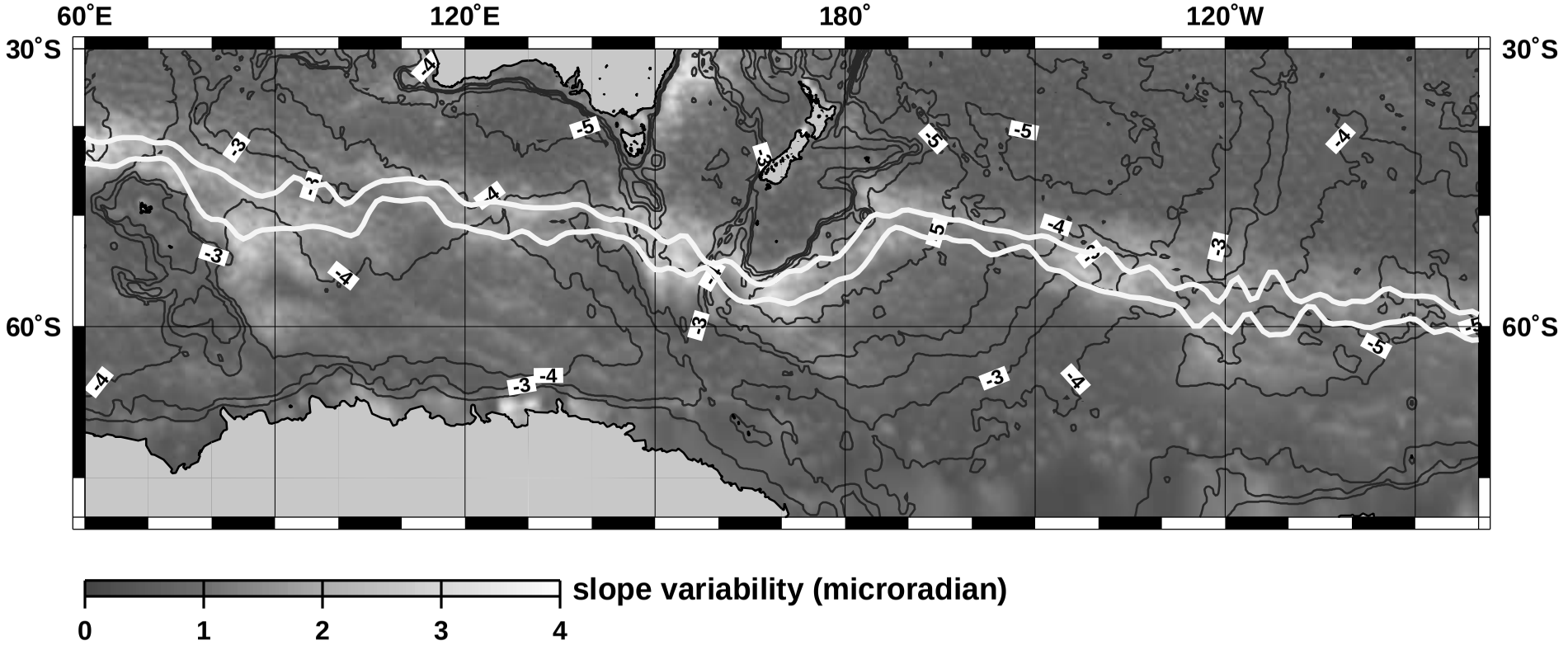
60˚E
120˚E
180˚
120˚W
30˚S
60˚S
slope variability (microradian)
0
1
2
3
4

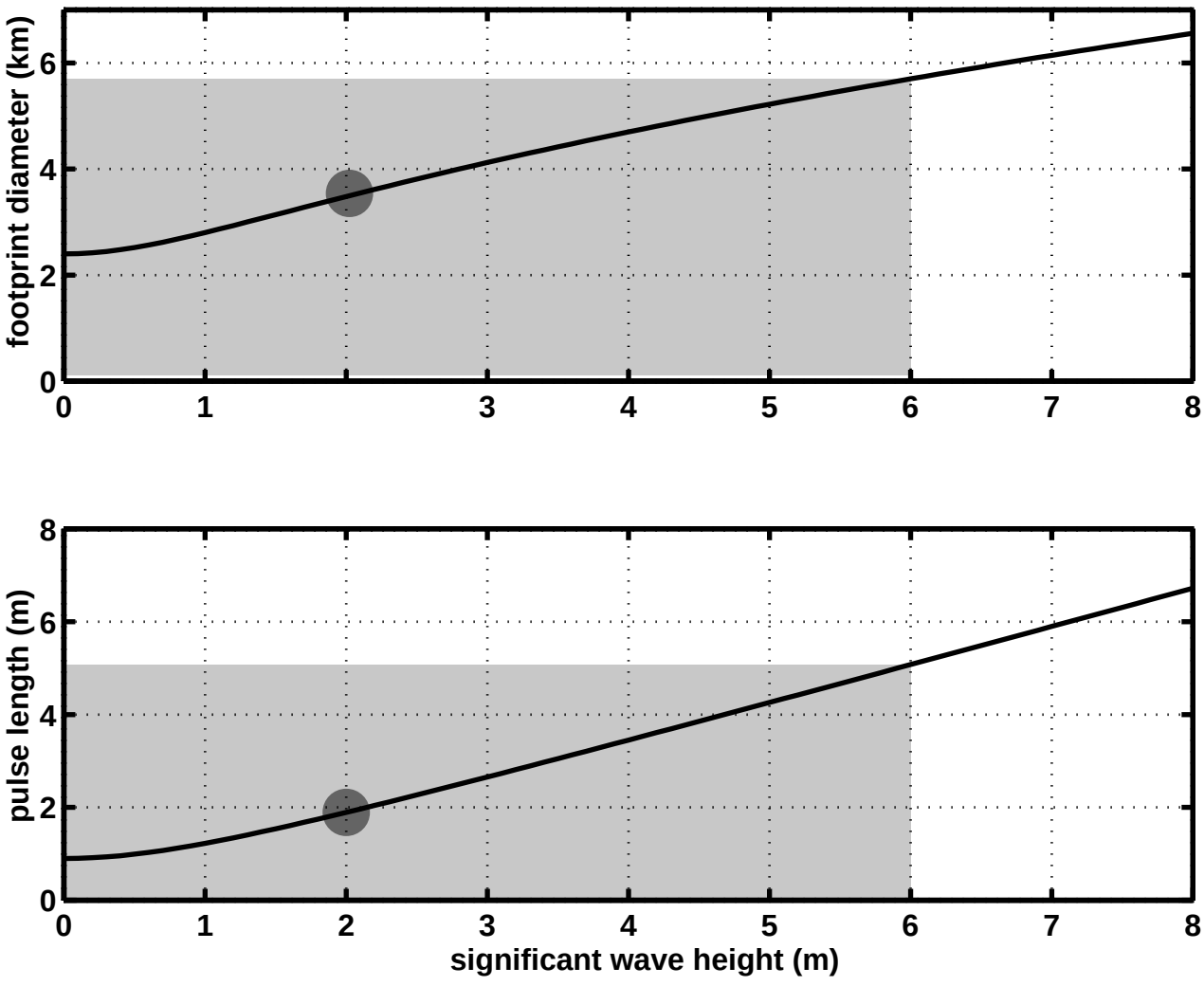
footprint diameter (km)
0
2
4
6
0
1
3
4
5
6
7
8
pulse length (m)
0
2
4
6
8
0
1
2
3
4
5
6
7
8
significant wave height (m)